Revised manuscript submitted to Geochimica et Cosmochimica Acta

13 March 2013

Dynamic Fe-precipitate formation induced by Fe(II) oxidation in aerated phosphate-containing water

Andreas Voegelin[a*], Anna C. Senn[a], Ralf Kaegi[a], Stephan J. Hug[a], Stefan Mangold[b]

[a] Eawag, Swiss Federal Institute of Aquatic Science and Technology, Ueberlandstrasse 133, CH-8600 Duebendorf, Switzerland.

[b] Karlsruhe Institute of Technology, Institute of Synchrotron Radiation, Hermann-von-Helmholtz Platz 1, D-76344 Eggenstein-Leopoldshafen, Germany

[*] Corresponding author. E-mail address: andreas.voegelin@eawag.ch, phone +41 58 765 54 70, fax +41 58765 52 10

ABSTRACT

We studied the effect of phosphate on the precipitation of Fe during the oxidation of 1 mM Fe(II) in aerated 8 mM $NaHCO_3$-CO_2 buffered aqueous solutions at near-neutral pH. The structure and morphology of the precipitates were analyzed by X-ray diffraction (XRD), extended X-ray absorption fine structure spectroscopy (EXAFS) at the Fe K-edge, and transmission electron microscopy (TEM). Most phosphate was incorporated into the Fe(III)-precipitates up to an initial dissolved P/Fe ratio of ~0.55. At dissolved P/Fe ratios from 0.55 to 1.91, the precipitate P/Fe ratios only exhibited a minor increase from 0.56 to 0.72. XRD patterns and Fe EXAFS spectra indicated a shift in precipitate type from mostly poorly-crystalline lepidocrocite in the absence of phosphate to amorphous Fe(III)-phosphate at dissolved P/Fe ratios >0.55. A time-resolved oxidation experiment at an initial dissolved P/Fe ratio of 0.29 revealed that amorphous Fe(III)-phosphate formed during Fe(II) oxidation until phosphate was nearly depleted from solution. During continuing Fe(II) oxidation, about half of the newly formed Fe(III) contributed to the polymerization of Fe-phosphate (mostly monomeric and oligomeric Fe(III)) into phosphate-rich hydrous ferric oxide with a maximum P/Fe ratio of 0.25 (HFO-P; edge-sharing linkage of Fe(III) octahedra) and about half precipitated as poorly-crystalline lepidocrocite in the phosphate-depleted solution. At initial P/Fe ratios <0.2, initially formed Fe(III)-phosphate was fully transformed into HFO-P during continuing Fe(II) oxidation. The dynamic interactions between phosphate and Fe described in this study impact the structure of fresh Fe(III)-precipitates at redox transitions in environmental and technical systems. The modulating effects of other dissolved species such as silicate and Ca on Fe precipitate formation and implications for co-transformed trace elements require further study.

1. INTRODUCTION

Iron and phosphate play central roles in a wide range of natural and engineered aquatic and terrestrial systems. Phosphate exhibits a high affinity for Fe and its biogeochemical cycle is therefore closely coupled to the cycle of Fe, which is strongly influenced by redox-transformations between relatively soluble ferrous Fe(II) and poorly soluble ferric Fe(III). During Fe(II) oxidation by O_2 and subsequent Fe(III) precipitation, interactions between Fe and phosphate can be especially pronounced. Fe(II) oxidation in aerated aqueous solutions initially leads to the formation of amorphous to poorly crystalline nanoscale Fe(III)-precipitates (Kaegi et al., 2010; Voegelin et al., 2010). Due to their high specific surface area and sorption capacity, these Fe(III)-precipitates are highly reactive and may act as mobile colloidal carriers or immobilizing solids for other elements, including toxic elements like arsenic or essential nutrients like phosphate (Mayer and Jarrell, 2000; Roberts et al., 2004). Conversely, phosphate also affects Fe(II) oxidation and Fe(III) precipitation in multiple interdependent ways. Phosphate accelerates the oxidation of dissolved Fe(II) (Mao et al., 2011; Tamura et al., 1976) and either accelerates (Cumplido et al., 2000) or slows down (Wolthoorn et al., 2004) oxidation of adsorbed Fe(II) in heterogenous systems. Phosphate also interferes with Fe(III) polymerization (Rose et al., 1996; Voegelin et al., 2010), promotes the formation of amorphous and crystalline Fe(III)-phosphates (Moore and Araki, 1977; Tessenow, 1974; Voegelin et al., 2010), and substantially retards the transformation of ferrihydrite into crystalline Fe(III)-oxides (including oxyhydroxides) (Galvez et al., 1999). Furthermore, via its influence on surface charge, phosphate may stabilize Fe(III)-precipitates against coagulation and settling (Gunnars et al., 2002; Tessenow, 1974), enhance the co-sorption of cations (for

example Cd (Venema et al., 1997)), and reduce the uptake of other oxyanions such as silicate, arsenate (As(V)) or arsenite (As(III)) (Roberts et al., 2004).

In spite of the rather detailed knowledge about individual phosphate-Fe interactions relevant over the course of Fe(II) oxidation and Fe(III) precipitation, the knowledge about their coupled temporal interplay and its consequences for the composition, structure and reactivity of fresh Fe(III)-precipitates forming in dilute aqueous solutions (i.e., at Fe concentrations relevant for typical ground- and soil pore waters) is still limited. The formation of phosphate-containing Fe(III)-precipitates by Fe(II) oxidation at near-neutral pH has been studied with respect to phosphate and colloidal Fe dynamics in aquatic systems (Einsele, 1938; Fox, 1989; Griffioen, 2006; Gunnars et al., 2002; Lienemann et al., 1999; Mayer and Jarrell, 2000; Tessenow, 1974) and As removal from drinking water (Hug et al., 2009; Meng et al., 2002; Roberts et al., 2004). Although these studies mostly focused on the extent of phosphate and As removal from solution, rather than on precipitate structure and formation mechanisms, two findings are of key importance with respect to the assessment of Fe(III)-precipitate formation in the presence of phosphate. First, phosphate (or arsenate) uptake per oxidized Fe was typically limited to ~0.5-0.6 P/Fe (Gunnars et al., 2002; Hug et al., 2009; Roberts et al., 2004; Tessenow, 1974), suggesting the formation of amorphous (basic) Fe(III)-phosphate at initial dissolved P/Fe ratios larger than ~0.5. Second, a limited number of time-resolved studies indicated that even during Fe(II) oxidation in solutions with initial dissolved P/Fe ratios less than ~0.5, a phosphate-rich precipitate with molar P/Fe ratio of ~0.5-0.6 forms first (Deng, 1997; Einsele, 1938; Gunnars et al., 2002; Tessenow, 1974). Based on the structural characterization of fresh Fe(III)-precipitates formed by Fe(II) oxidation in synthetic groundwater using X-ray absorption spectroscopy (XAS) and transmission electron microscopy (TEM) (Kaegi et al., 2010; Voegelin et al., 2010), we recently proposed that initial

formation of amorphous Fe(III)-phosphate in solutions with dissolved P/Fe ratios less than ~0.5 is followed by the formation of short-range-ordered to poorly-crystalline Fe(III)-(hydr)oxides in the phosphate-depleted solution. Sequential precipitate formation may have important implications with respect to the mechanism of Fe(III) precipitate formation in the presence of phosphate, since initially formed Fe(III)-phosphate may affect continuing Fe oxidation and precipitation after phosphate depletion and at the same time may be affected by reaction with remaining dissolved Fe(II) and polymerizing Fe(III). Furthermore, the different sequentially precipitating phases are likely to vary with respect to trace element incorporation and chemical and colloidal stability. In combination, these differences are likely to substantially influence the fate of Fe, phosphate and other elements over the course of Fe(II) oxidation in aquatic systems where P/Fe ratios may vary substantially (BGS and DPHE, 2001; Griffioen, 2006). This applies especially in systems where sequential precipitate formation leads to the spatially separated formation of different Fe(III)-precipitates, for example as a result of anoxic groundwater exfiltration into an oxic water body or along vertical redox gradients in stagnant water such as a lake's redoxcline.

To date, structural and mechanistic information on sequential Fe(III)-precipitate formation during Fe(II) oxidation in near-neutral aqueous solutions in the presence of phosphate is limited to our earlier XAS- and TEM-based studies (Kaegi et al., 2010; Voegelin et al., 2010) and was exclusively derived from the analysis of precipitates over a limited number of P/Fe ratios collected after complete Fe(II) oxidation. The aim of the present study therefore was to gain more detailed insights into the effect of phosphate on dynamic Fe(III)-precipitate formation during Fe(II) oxidation in aqueous solutions. Specifically, our objectives were (i) to determine the composition, structure and morphology of fresh Fe(III)-precipitates formed by Fe(II) oxidation at near-neutral pH as a function of initial dissolved P/Fe ratio and

(ii) to explore how the observed trends can be explained on the basis of the temporal interplay of interacting precipitate-forming processes. For this purpose, we performed several types of Fe(II) oxidation experiments at an environmentally relevant total Fe concentration of 1 mM. The initial dissolved P/Fe ratio was varied from 0 to 1.91 to cover the entire range from near-complete phosphate removal at P/Fe ratios from 0 to ~0.5 to Fe(III)-precipitate formation in the presence of excess phosphate at P/Fe ratios >0.6. To focus on phosphate-Fe interactions and to avoid confounding interferences from silicate or Ca (Griffioen, 2006; Mayer and Jarrell, 2000; Voegelin et al., 2010), all experiments were conducted in 8 mM $NaHCO_3$ background electrolyte adjusted to initial pH values of 7.0 or 6.3 using CO_2 gas. Initial solutions and unfiltered and filtered suspensions were analyzed for total Fe and P and precipitates were characterized by combining X-ray diffraction (XRD), Fourier-transform infrared spectroscopy (FTIR), X-ray absorption spectroscopy (XAS) at the Fe K-edge, transmission electron microscopy (TEM), and scanning TEM (STEM) combined with energy-dispersive X-ray detection (EDX).

2. MATERIALS AND METHODS

2.1. Fe(II) oxidation at variable P/Fe ratio with single Fe(II) addition (P/Fe series)

Experiments on Fe(III)-precipitate formation by Fe(II) oxidation in aerated solutions at 1 mM total Fe and variable initial P/Fe ratio (referred to as "P/Fe series" in this manuscript) were carried out in analogy to previous work (Roberts et al., 2004; Voegelin et al., 2010): Eight mM $NaHCO_3$ background electrolyte was prepared in high purity doubly deionized (DDI) water (18.2 MΩcm, Milli-Q® Element, Millipore). The pH was lowered to 5-6 by purging with CO_2 gas and was raised again to 7.0 (±0.1) using pressurized air to outgas CO_2. From the pH-adjusted background electrolyte, 150 mL were transferred into individual 250 mL

PET bottles. Phosphate was then added from a stock solution (100 mM $NaH_2PO_4 \times H_2O$) to obtain phosphate concentrations from 0 to 2 mM (see Table 1). The oxidation experiment was started by adding 1 mM Fe(II) from a concentrated stock solution (50 mM $FeSO_4 \times H_2O$, 1 mM HCl; prepared freshly for each experiment). After Fe(II) addition, the solutions were well agitated to ensure rapid mixing. The closed bottles were allowed to stand for 5 h, with about hourly remixing by slowly turning bottles upside down several times. Over time, the initially clear and colorless solutions turned brown to light-brown and turbid. After 5 h, pH had shifted from the initial value of 7.0 to ~7.3. Precipitates for XAS analysis were collected by passing ~150 mL of the suspensions through 0.2-μm cellulose acetate filters, followed by washing with 20 mL of DDI water and drying in air. For examination by transmission electron microscopy (TEM), ~20 μL of the precipitate suspension were deposited on a TEM grid (holey C, Cu grid) and drawn through the grid using a paper tissue. Subsequently, the grids were rapidly washed three times by immersion in DDI water. The precipitate powders and the TEM grids were stored in an exsiccator until analysis. From each experiment, 10 mL of unfiltered suspension were collected immediately after Fe(II) addition and 10 mL of final filtered suspension (0.2-μm nylon filters) were acidified to 0.65% HNO_3 for later analysis of Fe and P by inductively coupled plasma-mass spectrometry (ICP-MS). The amounts of P and Fe in the precipitates were calculated from their concentrations in the initial unfiltered and final filtered suspensions. For X-ray diffraction (XRD) analysis, Fourier-transform infrared spectroscopy (FTIR), and the gravimetric determination of dry precipitate mass, a second set of Fe(III)-precipitates was synthesized in larger solution volumes (1000 mL), otherwise following the described protocol (pH 7.0, 9 initial molar P/Fe ratios from 0 to 1.45).

To assess the effect of pH on precipitate P/Fe ratio, another series of precipitates was analogously synthesized in solutions initially adjusted to pH 6.3. Two hundred mL of the

background electrolyte were transferred into 250 mL PET bottles and adjusted to initial dissolved phosphate concentrations from 0 to 2 mM (10 levels). The oxidation experiment was started by spiking 1 mM Fe(II) to the phosphate-containing solutions. After 5 h, final pH values of ~6.5 were reached. Solution and precipitate samples were collected as described above.

2.2. Time-resolved Fe(II) oxidation experiment

To evaluate the temporal evolution of Fe(III)-precipitates during Fe(II) oxidation in the presence of phosphate, a time-resolved experiment was conducted at an initial dissolved P/Fe ratio of 0.29 and an initial pH of 6.3 at which Fe(II) oxidation was slow enough to enable time-resolved suspension and precipitate sampling. One L of 8 mM $NaHCO_3$ background electrolyte adjusted to pH 6.3 was prepared in a 1-L glass flask following the same procedure as described for the oxidation experiments in section 2.1. After addition of 0.3 mM phosphate, the experiment was started by the addition of 1 mM Fe(II). Unfiltered suspension was sampled just after Fe(II) addition for determination of the total initial concentrations of Fe and P by ICP-MS. During Fe(II) oxidation, the suspension was intensely stirred in the closed flask using a magnetic stirrer. At regular intervals up to a reaction time of 300 min, the flask was opened to remove about 100 mL of suspension. The pH was determined in unfiltered suspensions and aliquots of 10 mL of filtered suspension (0.2 µm nylon) were collected and acidified for analysis of dissolved Fe and P by ICP-MS. At selected sampling times, solids were collected for analysis by XAS and TEM as described for the P/Fe series. Filtered suspension collected after 60 min was allowed to further oxidize until the end of the experiment, at which time the precipitate and filtered suspension were sampled. Over the course of the experiment, the pH increased linearly from 6.3 at the time of Fe(II) addition to ~6.9 after 300 min due to CO_2 outgassing during repeated suspension removal (Fig. EA6d). In a replicate experiment, both

unfiltered and filtered suspension aliquots were collected over the entire experiment for the analysis of Fe an P by ICP-MS and of Fe_{tot} and Fe(II) by UV-Vis spectrometry.

2.3. Precipitate mixing experiment and sequential Fe(II) addition experiment

In the "mixing experiment", an Fe(III)-phosphate (P/Fe = 0.6) and a phosphate-free Fe(III)-precipitate were synthesized separately at pH 7.0 following the same protocol as described in section 2.1. After 5 h of oxidation, the suspensions were mixed in ratios of 50:50 and 25:75, resulting in suspensions with final P/Fe ratios of 0.3 and 0.15, respectively. The mixed suspensions were reacted for another 4 h prior to sample collection. Final pH values ranged between 7.0 and 7.5. In the "sequential Fe(II) addition experiment", two Fe(III)-phosphate suspensions with P/Fe of 0.6 with either 0.5 and 0.25 mM total Fe were prepared first (8 mM $NaHCO_3$, pH 7.0). After 5 hours, 0.5 or 0.75 mM Fe(II) was spiked to the two Fe(III)-phosphate suspensions, respectively, and allowed to oxidize for 4 h. This resulted in final suspensions with P/Fe ratios of 0.3 and 0.15 at 1 mM total Fe, i.e., the same as in the mixing experiment. Final pH values ranged between 7.0 and 7.5.

2.4. ICP-MS and UV-Vis colorimetry

Filtered and unfiltered suspension samples were acidified to 0.65% HNO_3 (Merck, suprapure). For the analysis of Fe, P and Na by ICP-MS (Agilent 7500ce), the samples were diluted as required and again acidified to 0.65% HNO_3. For determination of Fe(tot) and Fe(II) by UV-Vis colorimetry, samples were acidified to 0.75% HCl (to stabilize Fe oxidation state and to dissolve Fe-precipitates in unfiltered suspensions) and were analyzed following a published protocol (Fadrus and Malý, 1975) (Fe(II) within one h after sample collection, Fe(tot) within 1 day).

2.5. X-ray diffraction analysis and Fourier-transform infrared spectroscopy

For X-ray diffraction (XRD) analysis, 80 mg of the dried precipitates were suspended in ethanol and allowed to dry on 27-mm diameter low-background Si-slides. XRD patterns were recorded from 5 to 95° 2-θ with a step-size of 0.0167° and a measurement time of 4 h per sample using Co Kα radiation (X'Pert Powder diffractometer with XCelerator detector, PANanlytical, Almelo, The Netherlands). The same set of samples was analyzed by Fourier-transform infrared spectroscopy with attenuated total reflectance (Harrick Meridian diamond single reflection Split Pea ATR unit) on a Biorad FTS 575 C instrument with a liquid N_2-cooled MCT detector.

2.6. X-ray absorption spectroscopy

For Fe K-edge extended X-ray absorption fine structure (EXAFS) spectroscopy, appropriate amounts of the air-dried precipitates (~2-4 mg Fe) were mixed with ~150 mg cellulose and pressed into 13-mm pellets. Measurements at the XAS beamline at the Angströmquelle Karlsruhe (ANKA, Eggenstein-Leopoldshafen, Germany) were performed at room temperature in transmission mode using gas-filled ionization chambers. A double crystal monochromator (DCM) with a pair of Si(111) crystals was used for monochromatization. The energy was calibrated by setting the first inflection point of the K-shell absorption edge of a Fe foil to 7112 eV. Higher harmonics were rejected by detuning the incident photon beam to 70% of its maximum intensity using a software controlled D-Mostab (Struck, Germany).

Reference and sample spectra were processed and analyzed using the software code Athena (Ravel and Newville, 2005). The E_0 was fixed at 7128.5 eV. The spectra were normalized by subtracting a first-order polynomial fitted to the data from -100 to -30 eV before the edge and subsequently dividing through a second-order polynomial fitted to the data from

100 to 300 eV above the edge. EXAFS spectra were extracted using the Autobk algorithm (R_{bkg} = 0.9; *k*-weight = 3, spline *k*-range 0.5-11.9 Å^{-1}).

For the interpretation of the experimental spectra by linear combination fitting (LCF), four published reference spectra were used that we discussed in detail previously (Voegelin et al., 2010): Crystalline lepidocrocite (Lp) and goethite (Goe), short-range-ordered hydrous ferric oxide (HFO; labeled HFO-Si in (Voegelin et al., 2010)) and amorphous Fe(III)-phosphate (Fe-P; labeled Fe4-P4 in (Voegelin et al., 2010)). The HFO spectrum represents a hydrous ferric oxide synthesized by forced Fe(III) hydrolysis in the presence of silicate (Si). It contains about 0.5 Si/Fe and exhibits a similar degree of edge-sharing Fe-Fe linkage as 2-line ferrihydrite but a markedly lower degree of corner-sharing Fe-Fe linkage, which is suppressed by silicate (Voegelin et al., 2010) In the present study, silicate was not added in any of the experiments. However, LCF analyses including the HFO reference in general gave better results than if the spectrum of 2-line ferrihydrite was used instead (not shown). The HFO spectrum thus served to describe octahedrally coordinated Fe(III) with a certain degree of edge-sharing linkage, rather than a distinct silicate-containing Fe(III)-precipitate. The reference Fe-P represents an amorphous Fe(III)-phosphate with dominantly mono- and possibly oligomeric Fe(III) coordinated with phosphate.

Sample spectra were evaluated by LCF over the *k*-range 2-11 Å^{-1}. Starting with the best one-component fit, the number of components n was increased as long as the normalized sum of squared residuals (NSSR=($\sum$(data-fit)^2/$\sum$data^2)) of the best n+1-component was at least 10% (relative) lower than the NSSR of the best n-component fit. Neither individual fractions nor the sum of all fractions was constrained.

2.7. Transmission electron microscopy

To characterize precipitate morphology, the TEM (Tecnai, F30 STEM, FEI) was operated at 300 kV and images were recorded in bright field (BF) mode. For additional imaging and energy dispersive X-ray (EDX) analysis of two samples, an aberration-corrected dedicated scanning TEM (STEM; HD2700Cs, Hitachi, Japan) in combination with an EDX system (DX-4 with Genesis v6.20, EDAX, Mahwah, NJ, USA) was used. Images were recorded using a high-angle annular dark-field (HAADF) and secondary electron (SE) detectors. Elemental quantification was based on the Cliff-Lorimer thin-foil approximation (Williams and Carter, 2009). The peaks of P and Fe in the EDX spectra were fitted using Gauss functions after subtracting a linear background. The heights of the Gaussian peaks were taken as a measure for P and Fe signal intensities. From the P/Fe EDX intensity ratios ($(P/Fe)_{EDX}$) measured on a spatially homogeneous amorphous Fe(III)-phosphate with a known molar P/Fe ratio of 0.56 (sample P/Fe 0.58c, Table 1), an experimental $k_{P\text{-}Fe}$ factor was derived ($k_{P\text{-}Fe}$ = 0.87 ± 0.02 (s.d.; n=6); $k_{P\text{-}Fe}=(P/Fe)_{molar}/(P/Fe)_{EDX}$) that was used to convert measured P/Fe EDX intensity ratios into molar P/Fe ratios. For a phosphate-free Fe precipitate used as a blank control (sample P/Fe 0.00c; Table 1), a molar P/Fe ratio of 0.010 ± 0.004 (s.d.; n=6) was determined from EDX data.

3. RESULTS AND DISCUSSION

3.1. Precipitates formed at initial dissolved P/Fe ratios from 0 to 1.9 (P/Fe series)

3.1.1. Precipitate P/Fe versus initial dissolved P/Fe ratios

In the P/Fe series, we determined the P/Fe ratio, structure and morphology of Fe(III)-precipitates formed after single Fe(II) addition as a function of initial dissolved P/Fe ratio (data

for experiment at pH 7.0 provided in Table 1). The color of the fresh suspensions varied from orange at the lowest P/Fe ratios to beige at P/Fe ratios above 0.5 (Fig. EA1), suggesting a shift in precipitate structure. The molar P/Fe ratios of the Fe(III)-precipitates as a function of molar initial dissolved P/Fe ratio are shown in Fig. 1a. Up to a P/Fe ratio of 0.55, most phosphate was taken up by the Fe(III)-precipitates, as reflected by precipitate P/Fe ratios closely matching the initial dissolved P/Fe ratios. Higher initial dissolved P/Fe ratios from 0.55 up to 1.9 resulted only in a limited further increase of precipitate P/Fe ratios from 0.55 to ~0.7. Precipitates formed at pH 6.3 exhibited the same relationship between initial dissolved and final precipitate P/Fe ratios as precipitates formed at pH 7.0, also at initial dissolved P/Fe ratios > 0.55. This suggested that competition between Fe(III) hydrolysis and Fe(III)-phosphate complexation (Fox, 1989; Stumm and Sigg, 1979) did not significantly vary within this pH-range.

3.1.2. XRD patterns and FTIR spectra

The XRD patterns of Fe(III)-precipitates formed at pH 7.0 at initial dissolved P/Fe ratios from 0 to 1.45 are shown in Fig. 2. The XRD pattern of the precipitate formed in the absence of phosphate indicated dominantly lepidocrocite and a minor fraction of goethite. The peak widths reflected the nanocrystalline nature of the precipitates. For lepidocrocite, the differential broadening of the individual peaks was in line with earlier work and indicative for dominant crystallite growth along the corrugated octahedral sheets leading to the formation of lepidocrocite platelets (Schwertmann and Taylor, 1979). From the width of the 200 peak at 15.97° 2-θ, a crystallite size of about 3 nm perpendicular to the octahedral sheets was estimated (using the Scherrer equation), suggesting that lepidocrocite platelets consisted of about 5-6 octahedral sheets. The absence of goethite peaks in the XRD pattern of the precipitate formed at 0.03 P/Fe showed that even a small amount of phosphate effectively prevented goethite formation, in line with earlier work (Cumplido et al., 2000). Up to an initial

dissolved P/Fe ratio of 0.41, the height of the peaks of lepidocrocite drastically decreased, whereas a minor increase in peak width was only observed from 0 to 0.12 P/Fe (Fig. EA2). This suggested that increasing levels of phosphate effectively decreased lepidocrocite formation. whereas the effect on crystallite size was rather small. No lepidocrocite peaks were detected at P/Fe ratios of 0.50 and higher. Instead, the XRD patterns were dominated by a broad peak at 35.5° 2-θ corresponding to amorphous Fe(III)-phosphate (Thibault et al., 2009). The dry mass of the precipitates analyzed by XRD exhibited a systematic dependence on initial dissolved P/Fe ratio (Fig. EA3) and, for amorphous Fe(III)-phosphate formed at P/Fe ratios ≥0.5, was in line with the empirical stoichiometry $[FePO_4 \times 2H_2O]_x[Fe(OH)_3]_{(1-x)}$. The FTIR spectra of the same set of samples showed trends consistent with the XRD data (for details see Fig. EA4). Furthermore, they indicated that only 30 µM phosphate in the starting solution (P/Fe 0.03) effectively reduced carbonate uptake into the Fe(III)-precipitate from the 8 mM $NaHCO_3$ background electrolyte as compared to the phosphate-free precipitate. Thus, considering that high carbonate levels favor goethite over lepidocrocite formation (Carlson and Schwertmann, 1990), effective inhibition of goethite formation by phosphate at an initial dissolved P/Fe of 0.03 was probably related to its effect on carbonate uptake into the precipitate.

3.1.3. Fe K-edge EXAFS spectroscopy

The Fe K-edge EXAFS spectra of selected Fe(III)-precipitates from the P/Fe series at pH 7.0 and of references used for LCF analysis are shown in Fig. 3. The EXAFS spectra of all samples from the P/Fe series at pH 7.0 are shown in Fig. EA5 in the electronic annex. Comparison of the spectra of precipitates with P/Fe ratios from 0 to 0.72 to the reference spectra (Fig. 3) indicates a shift from predominantly lepidocrocite in phosphate-free solution to amorphous Fe(III)-phosphate at high P/Fe ratios, in line with XRD results (Fig. 2). This was

confirmed quantitatively by LCF analysis of the EXAFS spectra of all Fe(III)-precipitates formed at pH 7.0, as summarized in Table 1 and shown in Fig. 1b. The cumulative uncertainty from sample synthesis and XAS analysis was small as indicated by LCF results for replicate samples with (nearly) identical P/Fe ratios (Fig. 1b), with only a minor contribution from the statistical uncertainty of the LCF (see footnote b of Table 1). In the absence of phosphate, LCF analysis returned predominantly lepidocrocite and minor fractions of goethite and HFO. The lepidocrocite fraction decreased with increasing initial dissolved P/Fe ratio from 0 to 0.5, in close quantitative agreement with XRD results (Fig. EA2). Very small fractions of 0.04-0.05 goethite in the LCF of samples formed at P/Fe ratios from 0.06 to 0.12 did not visibly improve the fits, although they met the criteria to be included (see section 2.6), and were considered an artifact since goethite peaks were not observed in the corresponding XRD patterns (Fig. 2). Amorphous Fe(III)-phosphate was absent in the best LCF of samples with P/Fe <0.19. Above this P/Fe ratio, the Fe(III)-phosphate fraction strongly increased and reached 100% at precipitate P/Fe ratios ≥ 0.53 (Fig. 1c).

We previously suggested that in solutions with dissolved P/Fe ratios <0.55, Fe(III)-phosphate with a P/Fe ratio ~0.55 forms first until phosphate depletion (Voegelin et al., 2010), in line with macroscopic observations (Deng, 1997; Gunnars et al., 2002; Tessenow, 1974). Consequently, if the subsequently forming Fe(III)-precipitates are phosphate-free, the Fe(III)-phosphate fraction should linearly decrease from 100 to 0% as initial dissolved P/Fe decreases from ~0.55 to 0 (Fig. 1c, dashed red line). For initial dissolved P/Fe ratios from ~0.55 to 0.19, however, the LCF-derived Fe(III)-phosphate fractions decreased more rapidly, and no Fe(III)-phosphate was detected by LCF in samples formed at P/Fe ratios ≤0.14 (Fig. 1c). Since the evolution of suspension color during Fe(II) oxidation pointed to initial Fe-phosphate formation

at P/Fe ratios as low as 0.03 (Fig. EA1), these LCF results pointed to a structural transformation of the initially formed Fe(III)-phosphate.

The LCF analysis of three Fe(III)-precipitates formed in the absence of phosphate returned HFO fractions of 0.19-0.35 (Fig. 1b, Table 1). In these fits, the hydrous ferric oxide reference most likely accounted for the very low crystallinity of lepidocrocite (and goethite) compared to the well-crystalline lepidocrocite used as an EXAFS reference. Up to an initial dissolved P/Fe ratio of 0.14, on the other hand, the HFO fraction markedly increased while the lepidocrocite fraction decreased (Table 1), indicating the formation of a phosphate-related HFO precipitate. The LCF-derived HFO fractions were therefore differentiated into two sub-fractions: "HFO-pcl" related to the formation of poorly-crystalline lepidocrocite and goethite and "HFO-P" formed due to the presence of phosphate. To estimate HFO-pcl and HFO-P fractions, we assumed that the ratio (HFO-pcl)/(Lp+Goe) of precipitates formed in the presence of phosphate corresponded to the average (HFO)/(Lp+Goe) ratio of the 3 phosphate-free precipitates (see Table EA1). The results showed that HFO-P accounted for most (>75%) of the fitted HFO except at the lowest studied P/Fe ratios (Fig. 1d).

3.1.4. Electron microscopy

TEM images of Fe(III)-precipitates formed at pH 7.0 with precipitate P/Fe ratios of 0, 0.28, 0.56, and 0.12 are shown in Fig. 4a-c and 4i, respectively. At a P/Fe of 0, the Fe(III)-precipitate exhibits the "hedgehog-like" morphology (Cornell and Schwertmann, 2003) that we previously observed for lepidocrocite-rich precipitates formed under comparable conditions (Kaegi et al., 2010). The precipitate with a P/Fe 0.56, on the other hand, consists of significantly smaller spheroidal particles (colloids) with a smooth surface aggregated into fractal flocs, in line with previous results for amorphous Fe(III)-phosphate (Kaegi et al., 2010). At the intermediate P/Fe ratio of 0.28, the bright-field TEM image suggests that lepidocrocite

platelets have formed around spherical entities. The precipitate with P/Fe of 0.12 exhibited a similar morphology as the precipitate formed in phosphate-free solution. The morphology and local elemental composition of the precipitate P/Fe 0.12 was further examined by STEM-EDX (Fig. 5abc). The high-angle annular dark-field (HAADF) image (Fig. 5a) exhibited a similar morphology as the bright-field image (Fig. 4i) and reflected primarily the mass-thickness contrast of the sample, The secondary electrons (SE) image (Fig. 5b), which represents the surface morphology of the sample, revealed that the spherical entities (bright areas in Fig. 5a) were surrounded by loosely aggregated thin lepidocrocite platelets. In Fig 5g, molar P/Fe ratios derived from EDX measurements on several locations are compared to the bulk precipitate P/Fe ratio. Locations of type A1 corresponded to the centers of bright areas observed in HAADF images and exhibited P/Fe ratios that were significantly higher than the bulk P/Fe ratio (locally up to 0.20; despite possible bias by surrounding lepidocrocite platelets), suggesting that they corresponded to the transformation product of initially-formed Fe(III)-phosphate (visible during initial Fe(II) oxidation (Fig. EA1) but absent in the LCF of the precipitate after Fe(II) oxidation (Fig. 1c). For isolated lepidocrocite platelets (locations of type A2, Fig. 5c), on the other hand, P/Fe ratios as low as 0.022 were found. These lowest values fall into the range of reported phosphate sorption capacities of lepidocrocite at near-neutral pH (0.015 P/Fe) (Borggaard, 1983; Madrid and De Arambarri, 1985) or the maximum for structural phosphate incorporation (0.025 P/Fe) (Cumplido et al., 2000). Higher P/Fe ratios measured on other lepidocrocite crystals may have resulted from the excitation of nearby phosphate-rich zones by scattered electrons.

3.2. Time-resolved Fe(II) oxidation and precipitate formation at P/Fe of 0.29

The XAS and TEM results for precipitates formed at initial dissolved P/Fe ratios from 0 to 1.91 suggested that initial Fe(III)-phosphate formation in phosphate-containing solutions

may be followed by the structural transformation of the Fe(III)-phosphate phase in parallel to concomitant lepidocrocite formation. To further explore the temporal evolution of Fe(III)-precipitates during Fe(II) oxidation in the presence of phosphate, a time-resolved experiment was conducted at an initial dissolved P/Fe ratio of 0.29 and an initial pH of 6.3.

3.2.1. Dynamics of dissolved Fe and phosphate and precipitate composition

The dissolved concentrations of Fe and P and the P/Fe ratio of the precipitate retained on the filter membranes as a function of reaction time are shown in Fig. 6ab. The data clearly confirm that Fe(II) oxidation initially results in the precipitation of a phosphate-rich Fe-precipitate whose P/Fe ratio reaches ~0.52 at the time of near-complete phosphate depletion from solution (~60 min after Fe(II) addition). In a replicate experiment, unfiltered and filtered suspensions collected over the course of Fe(II) oxidation were photometrically analyzed for Fe(II) and total Fe (details in electronic annex; Fig. EA3 and Fig. EA7). The results confirmed that the Fe that passed the filter membranes was nearly exclusively Fe(II) (within analytical accuracy), suggesting that it was mostly truly dissolved. For the precipitate retained on the filter membrane, on the other hand, the results indicated that 60 min after Fe(II) addition, i.e., at the time of phosphate depletion, about 15% of the precipitated Fe were Fe(II). The log-scale plot of dissolved Fe and P (Fig. 6a) suggests a marked increase in the rate coefficient of dissolved Fe (i.e., dissolved Fe(II)) disappearance at the time where phosphate is nearly depleted from solution, indicating an increase of the Fe(II) oxidation rate coefficient. The relatively small pH increase over the period of phosphate depletion (around 60 min; Fig. EA6) and the fact that heterogeneous Fe(II) oxidation is less pH-dependent than homogeneous oxidation (Cumplido et al., 2000) suggest that pH was not the main factor that led to enhanced Fe(II) oxidation.

Linear regression of the log-transformed dissolved Fe concentration (not shown) suggested an increase of the pseudo-first-order oxidation rate coefficient by a factor of about 2.3 at the time of phosphate depletion, in reasonable agreement with a 2.6 times higher rate coefficient for autocatalytic Fe(II) oxidation in phosphate-free solution compared to phosphate-containing solution (at dissolved P/Fe 0.74 resulting in exclusive Fe(III)-phosphate formation) (Wolthoorn et al., 2004). This strongly suggested that the increase of the apparent Fe(II) oxidation rate coefficient was due to the transition from Fe(III)-phosphate precipitation to formation of Fe(III)-(hydr)oxides with higher autocatalytic activity.

Dissolved phosphate was observed to slowly increase again after ~120 min of reaction (Fig. 6a), i.e., at the time where Fe(II) oxidation approached completion (Fig. EA6). This probably reflects ongoing Fe(III) polymerization after Fe(II) oxidation was completed and no more Fe(III) was added to the precipitate phase. Although the increase in pH from ~6.7 at 150 min to ~6.9 at the end of the oxidation experiment (Fig. EA6) may have promoted desorptive phosphate release, this effect was probably of minor importance, considering the rather small effect of pH on phosphate adsorption to ferrihydrite within this pH range (Arai and Sparks, 2001).

3.2.2. EXAFS spectroscopy and electron microscopy

Precipitates for analysis by XAS and TEM were collected after 60 and 300 min reaction time (p-0-60 and p-0-300, respectively, Fig. 6a), as well as from filtrate collected after 60 min and allowed to further oxidize until 300 min (p-60-300, Fig. 6a). The corresponding EXAFS spectra are shown in Fig. 3, LCF results are displayed in Fig. 6c (complete results in Table 2), and TEM images in Fig. 4cde. Both XAS and TEM confirmed the formation of an amorphous Fe(III)-phosphate precipitate within the first 60 min of Fe(II) oxidation, in line with the temporal evolution of suspension color (Fig. EA8). However, it should be noted that the

suspended precipitate contained ~15% Fe(II) (see Fig. EA7) that were oxidized during sample drying. The precipitate collected at the end of the experiment closely resembled the precipitate with P/Fe 0.28 from the P/Fe series, both with respect to its local Fe coordination (XAS) and morphology (TEM). For the precipitate formed in the phosphate-free filtrate from 60-300 min, XAS (Fig. 3, 4c) and TEM (Fig. 4e) returned nearly identical results as obtained for the phosphate-free Fe(III)- precipitate from the P/Fe series (Fig. 1b, Fig 3b). The comparison of the morphology of the precipitates p-0-60, p-60-300 and p-0-300 (Fig. 4d-f) clearly showed that the final precipitate p-0-300 was not simply the sum of the two precipitates p-0-60 and p-60-300 (i.e., Fe(III)-phosphate and phosphate-free Fe(III)-(hydr)oxide). LCF analysis of the precipitate p-0-300 returned lower fractions of Fe(III)-phosphate and lepidocrocite and a higher fraction of HFO as compared to the simple addition (c-0-300) of the corresponding fractions of the precipitates p-0-60 and p-60-300 (Fig. 6c). This suggested that part of the initially formed Fe(III)-phosphate (p-0-60) was transformed during continuing Fe(II) oxidation (and possibly subsequent aging) to phosphate-rich HFO (HFO-P) with higher degree of Fe(III) polymerization. To quantify this transformation, we calculated the "difference LCF" c-60-300 between the precipitates p-0-60 and p-0-300 (Fig. 6c, see also footnote c in Table 2) which describes the structural change per Fe(II) oxidized from 60 to 300 min. The result indicated that for each Fe(II) oxidized after dissolved phosphate depletion, about 0.4 Fe-phosphate together with about half of the newly formed Fe(III) transformed into a precipitate with HFO-like local Fe coordination while the other half of the newly formed Fe(III) precipitated as lepidocrocite. Hence, assuming a P/Fe ratio of 0.55 for initially forming Fe(III)-phosphate, the LCF results from the time-resolved experiment suggested that complete Fe(III)-phosphate transformation could be expected for initial dissolved P/Fe ratios ≤0.157, in excellent agreement with LCF results obtained from the P/Fe series (Fig. 1bc).

3.3. Precipitate mixing and sequential Fe(II) addition experiments

To test if Fe(III)-phosphate transformation over the timescale of our experiments (4-5 h) mainly occurred during ongoing Fe(II) oxidation after phosphate depletion or during subsequent aging (2-3 h) prior to sample collection, we conducted two experiments: (i) In the mixing experiment, freshly formed Fe(III)-phosphate was reacted for 4 h with fresh phosphate-free Fe(III)-(hydr)oxide. (ii) In the sequential Fe(II) addition experiment, Fe(II) was spiked to freshly formed Fe(III)-phosphate in aerated suspension and the precipitate was examined after 4 h reaction time. In both experiments, the final suspensions had total P/Fe ratios of ~0.30 and ~0.15 at 1 mM total Fe. To quantify changes in Fe coordination induced by Fe addition to fresh colloidal Fe(III)-phosphate, difference EXAFS spectra were calculated by subtracting the normalized XAS spectrum of the initial amorphous Fe(III)-phosphate from the normalized XAS spectra of the final precipitates, using weighing factors to account for the respective amounts of Fe (Table 3). The results from the LCF analysis of the difference spectra are listed in Table 3 and shown in Fig. 7 (sample, difference and LCF spectra in Fig. EA9).

For the mixing experiment, TEM image of the sample Mix 0.15 (Fig. 4g) clearly revealed an aggregate of Fe(III)-phosphate and phosphate-free Fe(III)-precipitate that did not show apparent morphological alteration compared to the respective starting materials (Fig. 4ac). Accordingly, the LCF of the difference spectra (d-Mix 0.15; d-Mix 0.30) closely matched the LCF of the added phosphate-free Fe(III)-precipitate (P/Fe 0.00c; Table 3, Fig. 7). In combination, these TEM and XAS results suggested that the analysis of difference spectra correctly reproduced the spectral changes induced by Fe addition to Fe(III)-phosphate suspension, and that Fe(III)-phosphate was not dissolved or transformed to a significant extent when reacted for 4 h with phosphate-free Fe(III)-(hydr)oxide that could act as a phosphate sink.

In contrast, the LCF results for the sequential Fe(II) addition experiment indicated that the second Fe(II) spike resulted in the partial transformation of Fe(III)-phosphate into HFO (Fig. 7), demonstrating that Fe(III)-phosphate transformation over the timescale of our experiments was coupled to continuing Fe(II) oxidation. The sample Seq 0.15 with final P/Fe ratio of 0.13 (Fig. 4h) exhibited a similar morphology as the sample P/Fe 0.12 from the P/Fe series (Fig. 4i), which formed after a single Fe(II) spike. Spatially-resolved analysis of the precipitate Seq 0.30 by STEM-EDX (Fig. 5def) showed that isolated lepidocrocite platelets had very low P/Fe ratios (Fig. 5g, locations of type B2) as observed for the precipitate P/Fe 0.12, In contrast, bright areas in the center of aggregates (type B1) observed in HAADF images (Fig. 5d) exhibited P/Fe ratios from 0.56 down to 0.38 (Fig. 5g), suggesting that they corresponded to partly transformed colloidal Fe(III)-phosphate. Complementary HAADF and SE images recorded on sample Seq 0.30 (Fig. 5de) showed thin lepidocrocite platelets attached to the surface of Fe(III)-phosphate/HFO-P particles, as observed for precipitate P/Fe 0.12 (Fig. 5ab).

3.4. Formation of amorphous Fe(III)-phosphate

Precipitates with P/Fe ratios of 0.53 to 0.72 formed at initial dissolved P/Fe ratios >0.55 were identified as amorphous Fe(III)-phosphate using XRD (Fig. 2), XAS (Fig. 1 and 3) and TEM (Fig. 4). The dry mass of these basic Fe(III)-phosphates was well described by the empirical stoichiometry $[Fe(PO_4)_3{\times}2H_2O]_x[Fe(OH)_3]_{(1-x)}$, x denoting the precipitate P/Fe ratio (Fig. EA3). Their nearly identical EXAFS spectra (Fig. EA5) suggested that local Fe coordination did not vary significantly despite the variation in P/Fe ratio from 0.53 to 0.72. The structural interpretation of the Fe K-edge EXAFS spectra of amorphous Fe(III)-phosphates is not unambiguous, but clearly indicates that Fe(III) polymerization is limited to the stage of monomers and small oligomers (Voegelin et al., 2010). Similarly, local Fe coordination in

amorphous Fe(III)-arsenate formed at more acidic pH has been proposed to be dominated by monomeric Fe in scorodite-like local coordination (Chen et al., 2009) or by single corner-sharing Fe chains bridged by arsenate (Paktunc et al., 2008). Irrespective of the effective average local Fe coordination in amorphous Fe(III)-phosphate, our results for precipitates from the P/Fe series indicate that - at near-neutral pH of 6.3 to 7.0 - a precipitate P/Fe ratio of at least ~0.55 is required to prevent Fe(III) polymerization into larger units such as octahedral double-chains or sheets during Fe(II) oxidation.

Amorphous Fe(III)-phosphate with a P/Fe ratio of unity can be synthesized at low pH and high dissolved P/Fe ratio (Hsu, 1973; McLaughlin and Syers, 1978) (the same also applies to amorphous Fe(III)-arsenate (Paktunc et al., 2008)). Higher pH and lower P/Fe ratios are expected to result in the formation of basic Fe(II/III)-phosphates with lower P/Fe ratios (Fox, 1989; Stumm and Sigg, 1979). Many Fe(II/III)-(hydroxy)phosphates, including vivianite and its oxidation products metavivianite and amorphous santabarbaraite (Pratesi et al., 2003) exhibit a low degree of Fe-Fe coordination and a P/Fe ratio of 0.67. This value compares to the highest P/Fe ratios in the P/Fe series (Fig. 1a) and the P/Fe ratio of the initially forming precipitate in the time-resolved experiment (Fig. 6b), and is likely to represent the maximum P/Fe ratio of amorphous Fe(III)-phosphates at near-neutral pH. Higher precipitate P/Fe ratios at near-neutral pH may however be observed in the case of enhanced co-precipitation of phosphate and Ca with Fe (Griffioen, 2006; Voegelin et al., 2010).

In the experiments presented in this study, addition of 1 mM Fe(II) to aerated phosphate-containing solutions induced Fe(II) oxidation, but at the same time caused initial oversaturation of vivianite. We did not observe the precipitation of vivianite in any of our experiments, but Fe(II) concentrations in unfiltered and filtered suspensions from the time-resolved experiment (Fig. EA7) indicated Fe(II)-fractions of ~23 and ~16% in precipitates after reaction times of 30

and 60 min, the latter corresponding to the Fe-phosphate precipitate at the time of phosphate depletion from solution. Thus the precipitate formed during initial Fe(II) oxidation was a mixed Fe(II/III)-phosphate that underwent rapid heterogeneous oxidation to amorphous Fe(III)-phosphate concomitant with continuing oxidation of dissolved Fe(II).

Analysis of the precipitate p-0-60 from the time-resolved experiment by XAS (Fig. 6) and TEM (Fig. 4) demonstrated that amorphous Fe(III)-phosphate precipitated first even at an initial dissolved P/Fe ratio less than 0.55, confirming earlier macroscopic observations (Deng, 1997; Einsele, 1938; Gunnars et al., 2002; Roberts et al., 2007; Tessenow, 1974) and our earlier conclusion from a limited set of spectroscopic and microscopic observations (Kaegi et al., 2010; Voegelin et al., 2010). Furthermore, the evolution of suspension color in the P/Fe series indicated initial Fe(III)-phosphate precipitation down to the lowest tested P/Fe ratio of 0.03 (Fig. EA1). On the other hand, the XAS results from the P/Fe series and the time-resolved experiment revealed that initially formed Fe-phosphate was subject to subsequent structural transformation, resulting in the absence of Fe(III)-phosphate in final precipitates formed at initial dissolved P/Fe ratios ≤0.16.

3.5. Transformation of Fe(III)-phosphate into HFO-P during Fe(II) oxidation

The XAS results for precipitates from the P/Fe series (Fig. 1d) and the time-resolved experiment (Fig. 6c) in combination with the identification of phosphate-rich domains by STEM-EDX in the precipitate P/Fe 0.12 from the P/Fe series (Fig. 5ag) and the precipitate Seq 0.30 (Fig. 5dg) suggested that initially formed Fe(III)-phosphate became gradually transformed into phosphate-rich HFO-P. The mixing and sequential Fe(II) addition experiments (Fig. 7) further showed that, on the timescale of our experiments, this transformation mainly occurred during continuing Fe(II) oxidation rather than after Fe(II) oxidation. Most probably Fe(III)-phosphate transformation to HFO-P was due to Fe(II) oxidation on the surface or within

hydrated colloidal Fe(III)-phosphate. By decreasing the P/Fe ratio to less than ~0.55, this leads to the gradual polymerization and transformation of Fe(III)-phosphate into HFO-P. During Fe(II) oxidation, adsorbed Fe(II) may have catalyzed phase transformations via an electron transfer mechanism (Frierdich and Catalano, 2012; Jones et al., 2009; Pedersen et al., 2005; Williams and Scherer, 2004). However, considering that co-precipitated phosphate may act similarly to silicate which stabilizes Si-rich ferrihydrite against Fe(II)-induced transformation to lepidocrocite (Jones et al., 2009) and that net Fe(III) addition was needed to drive the polymerization process, electron transfer from adsorbing Fe(II) was probably of minor relevance with respect to Fe(III)-phosphate transformation to HFO-P.

We previously showed that silicate-rich HFO may form by Fe(II) oxidation at dissolved Si/Fe ratios >0.5 (Voegelin et al., 2010), with silicate suppressing Fe(III) polymerization via corner-sharing linkage (Doelsch et al., 2000; Pokrovski et al., 2003). The present study indicates that an analogous phosphate-rich HFO with similar degree of Fe(III) polymerization can form by transformation of initially formed Fe(III)-phosphate during continuing Fe(II) oxidation. Based on phosphate sorption capacities of 0.015 P/Fe for lepidocrocite (Borggaard, 1983; Madrid and De Arambarri, 1985), a maximal structural phosphate uptake of 0.025 P/Fe (Cumplido et al., 2000), and our STEM-EDX data which indicated low P/Fe ratios for lepidocrocite in our samples (Fig. 5cfg), we considered phosphate uptake by lepidocrocite in our experiments to be small relative to phosphate uptake by Fe(III)-phosphate and HFO-P. Thus, assuming that all phosphate in the precipitate was associated with Fe(III)-phosphate/HFO-P and that Fe(III)-phosphate contained 0.55 P/Fe, a P/Fe ratio of 0.25 ± 0.07 (s.d., n=11) was calculated for the HFO-P fraction in precipitates formed at initial dissolved P/Fe ratios from 0.03 to 0.42 (Table EA1). Essentially the same P/Fe ratio (0.24 ± 0.05 (s.d., n=6)) was obtained for the entire HFO fraction of samples formed at P/Fe ratios from 0.14 to

0.42 (where LCF-derived HFO was mostly HFO-P (Fig. 1d) and phosphate was sufficiently high to saturate the HFO; Table EA1). These values are in excellent agreement with adsorption maxima of 0.26 P/Fe (pH 6) and 0.24 As(V)/Fe (pH 8.0) reported for freshly-precipitated ferrihydrite (Fuller et al., 1993; Gerke, 1993).

From the time-resolved experiment (Fig. 6), we concluded that per Fe(II) oxidized after Fe(III)-phosphate formation, ~0.40 Fe from Fe(III)-phosphate was transformed into HFO-P. Taking the P/Fe ratios of Fe(III)-phosphate and HFO-P and the mass-balance for Fe and P into account, this requires that about half (48%) of the Fe(II) oxidized during this continuing Fe(II) oxidation entered the HFO-P while the other half (52%) precipitated as (nearly) phosphate-free precipitate (i.e., lepidocrocite and related HFO-pcl according to EXAFS classification). This result is in perfect agreement with XRD and XAS results showing that lepidocrocite also formed at P/Fe ratios from 0.2 to 0.4 where the transformation of Fe(III)-phosphate to HFO-P was not completed after Fe(II) oxidation, as well as with TEM images showing lepidocrocite platelets on the surface of phosphate-rich Fe(III)-phosphate/HFO-P particles (Fig. 5be).

3.6. Precipitate transformation after Fe(II) oxidation

In the time-resolved experiment, dissolved phosphate started to slowly increase again after most Fe(II) had been oxidized (Fig. 6a and Fig. EA6; from 120 to 300 min). This increase was too small to significantly decrease the precipitate P/Fe ratio, but demonstrated the immediate onset of precipitate aging after complete Fe(II) oxidation. This can be attributed to ongoing Fe(III) polymerization combined with no further Fe(III) supply to the solid phase that could have retained phosphate. In earlier work, aging of a fresh Fe(III)-derived precipitate with an As(V)/Fe ratio of 0.19 for 33 days was found to release about 37% of the initially co-precipitated As(V) (Fuller et al., 1993). Similarly, about 38% of the phosphate adsorbed to freshly-prepared ferrihydrite at a maximum loading of 0.26 P/Fe at pH 6 was released back

into solution within 38 days of aging (Gerke, 1993). Under conditions similar to our experiments (5 mM $NaHCO_3$, pH 7.0, 0.1 mM Fe(II)), Mayer and Jarrell (2000) performed an Fe(II) oxidation and precipitate aging experiment at an initial dissolved P/Fe 0.2. Over 10-15 days of aging, the authors observed ~75% phosphate release back into solution, resulting in a P/Fe of only ~0.05 of the aged Fe(III)-precipitate. This result suggests that also phosphate-saturated HFO formed by transformation of Fe(III)-phosphate continues to polymerize into (crystalline) Fe(III)-(hydr)oxides with concomitant phosphate release. On the other hand, solutes such as silicate or humic acid interfere with Fe(III) polymerization and may markedly slow down Fe(III) polymerization, phase transformation and associated phosphate release (Gerke, 1993; Mayer and Jarrell, 2000).

3.7. Conceptual model for Fe(III)-precipitate formation by Fe(II) oxidation in the presence of phosphate

Based on the minimal P/Fe ratio of amorphous Fe(III)-phosphate (0.55), the P/Fe ratios of phosphate-saturated HFO-P (0.25) and the finding that about 0.4 Fe(III)-phosphate is transformed into HFO-P per Fe(II) oxidized after phosphate depletion, and taking the temporal sequence of precipitate formation into account, we can rationalize Fe(III)-precipitate formation by Fe(II) oxidation in the presence of phosphate as a 3-step process, where the initial molar ratio of dissolved phosphate over Fe(II) determines how Fe(III)-precipitate formation in a closed system proceeds (Figure 8). (i) In the first step, Fe(III)-phosphate with a minimum P/Fe ratio of 0.55 forms. At initial dissolved P/Fe ratios > 0.55, amorphous Fe(III)-phosphate is the only product of Fe(II) oxidation (Fig. 8f). (ii) At initial dissolved P/Fe ratios < 0.55, initial Fe(III)-phosphate formation leads to the depletion of dissolved phosphate on a linear scale (Fig. 6a). Continuing Fe(II) oxidation results in Fe(III)-phosphate transformation into HFO-P and concomitant precipitation of lepidocrocite (including HFO-pcl), with about half of the

newly formed Fe(III) sequestering into HFO-P and about half into lepidocrocite (Fig. 8d). At an initial dissolved P/Fe ratio of ~0.16, this process results in complete Fe(III)-phosphate transformation into HFO-P (Fig. 8d). (iii) At initial dissolved P/Fe ratios <0.16, continuing Fe(II) oxidation after complete Fe(III)-phosphate transformation to HFO-P results in the exclusive precipitation of lepidocrocite (including HFO-pcl) (Fig. 8b). This sequence determines Fe(III)-precipitate structure at the end of Fe(II) oxidation as a function of initial dissolved P/Fe ratio (Fig. 8g). As discussed in section 3.6, precipitate structure will be subject to further changes during subsequent aging. In the present study, we visually observed Fe-phosphate formation at P/Fe ratios as low as 0.03. Considering that about 0.015 to 0.025 P/Fe may be sorbed or occluded in lepidocrocite (Borggaard, 1983; Cumplido et al., 2000; Madrid and De Arambarri, 1985), however, precipitate formation at P/Fe ratios below 0.03 may deviate from the sequential precipitate formation described in Fig. 8. Finally, it should be noted that the sequence of precipitate formation and transformation described in the present study applies to near-neutral Na-bicarbonate buffered aqueous solutions. Variations are expected in the presence of other solutes such as Ca, Si or humic acid.

3.8. Environmental implications

This study demonstrates that Fe precipitation during Fe(II) oxidation in the presence of phosphate is a more complicated process than simple formation of a Fe(III)-(hydr)oxide coupled with competitive ion adsorption, and that several types of precipitates may form and transform over the course of Fe(II) oxidation. Different Fe(III)-precipitate types may exhibit different sorption affinities for co-transformed trace elements, both cations and anions. They are also expected to vary with respect to their colloidal stability which is strongly affected by adsorbed or co-precipitated phosphate (Gunnars et al., 2002). Variations in the adsorption affinity of Fe(II) to different Fe(III)-precipitates as well as differences in their autocatalytic

activity may have a significant impact on the rate of heterogeneous Fe(II) oxidation (Tamura et al., 1980; Wolthoorn et al., 2004) and probably also on the coupled oxidation rates of trace elements such as As(III) (Hug and Leupin, 2003).

A temporal sequence of Fe precipitate formation can be expected for anoxic waters containing Fe(II) and phosphate when brought into contact with O_2, either by aeration - for example in drinking water treatment for As removal or - or by mixing with oxygenated water - for example by exfiltration of anoxic groundwater into oxic surface water. In both cases, this temporal sequence may translate into spatially separated formation of different types of Fe(III)-precipitates along subsurface or surface flow paths. Spatial gradients may also develop as a result of diffusive solute transport, for example at the redoxcline in lakes. In such systems, localized formation of Fe-phosphate may result from partial Fe(II) oxidation at low O_2 partial pressures at the reducing boundary of the redoxcline, even in waters with low P/Fe ratios. Spatial variations in precipitate structure may also occur at much smaller scales of millimeters to nanometers, for example as a result of localized oxidant release by plant roots (Voegelin et al., 2007) or microorganisms (Miot et al., 2009).

This study focused on the dynamics of Fe oxidation and precipitation at near-neutral pH in the presence of phosphate, excluding the confounding effects of solutes like Ca, silicate, or humic and fulvic acids. Further work is required to quantify their effects on Fe oxidation, precipitation, and precipitate aging and the resulting impact on co-transformed trace elements.

4. ACKNOWLEDGEMENTS

The Angströmquelle Karlsruhe (ANKA, Karlsruhe, Germany) is acknowledged for the provision of synchrotron XAS beamtime, and the Electron Microscopy Centre of the ETH Zurich (EMEZ) for access to electron microscopes. Thomas Rüttimann and Irene Brunner

(Eawag) are acknowledged for assistance with laboratory experiments and analyses. This project was financially supported by the Swiss National Science Foundation under contract No. 200021-132123.

5. REFERENCES

Arai, Y. and Sparks, D. L., 2001. ATR-FTIR spectroscopic investigation on phosphate adsorption mechanisms at the ferrihydrite-water interface. *J. Colloid Interface Sci.* **241**, 317-326.

BGS and DPHE, 2001. Arsenic contamination of groundwater in Bangladesh. In: Kinniburgh, D. G. and Smedley, P. L. Eds.)*British Geological Survey Technical Report WC/00/19. 4 Volumes*. British Geological Survey (BGS) & Bangladesh Department for Public Health Engineering (DPHE), Keyworth, UK.

Borggaard, O. K., 1983. Effect of surface area and mineralogy of iron oxides on their surface charge and anion-adsorption properties. *Clays Clay Min.* **31**, 230-232.

Carlson, L. and Schwertmann, U., 1990. The effect of CO_2 and oxidation rate on the formation of goethite versus lepidocrocite from an Fe(II) system at pH 6 and 7. *Clay Minerals* **25**, 65-71.

Chen, N., Jiang, D. T., Cutler, J., Kotzer, T., Jia, Y. F., Demopoulos, G. P., and Rowson, J. W., 2009. Structural characterization of poorly-crystalline scorodite, iron(III)-arsenate co-precipitates and uranium mill neutralized raffinate solids using X-ray absorption fine structure spectroscopy. *Geochim. Cosmochim. Acta* **73**, 3260-3276.

Cornell, R. M. and Schwertmann, U., 2003. *The Iron Oxides*. Wiley-VCH, Weinheim.

Cumplido, J., Barron, V., and Torrent, J., 2000. Effect of phosphate on the formation of nanophase lepidocrocite from Fe(II) sulfate. *Clays Clay Min.* **48**, 503-510.

Deng, Y., 1997. Formation of iron(III) hydroxides from homogeneous solutions. *Water Research* **31**, 1347-1354.

Doelsch, E., Rose, J., Masion, A., Bottero, J. Y., Nahon, D., and Bertsch, P. M., 2000. Speciation and crystal chemistry of iron(III) chloride hydrolyzed in the presence of SiO4 ligands. 1. An Fe K-edge EXAFS study. *Langmuir* **16**, 4726-4731.

Einsele, W., 1938. Über chemische und kolloidchemische Vorgänge in Eisen-Phosphat-Systemen unter limnochemischen und limnogeologischen Gesichtspunkten. *Arch. Hydrobiol.* **33**, 361-387.

Fadrus, H. and Malý, J., 1975. Suppression of iron(Ill) interference in the determination of iron(lI) in water by the 1,10-phenanthroline method. *Analyst* **100**, 549-554.

Fox, L. E., 1989. A model for inorganic control of phosphate concentrations in river waters. *Geochim. Cosmochim. Acta* **53**, 417-428.

Frierdich, A. J. and Catalano, J. G., 2012. Controls on Fe(II)-activated trace element release from goethite and hematite. *Environ. Sci. Technol.* **46**, 1519-1526.

Fuller, C. C., Davis, J. A., and Waychunas, G. A., 1993. Surface chemistry of ferrihydrite: Part 2. Kinetics of arsenate adsorption and coprecipitation. *Geochim. Cosmochim. Acta* **57**, 2271-2282.

Galvez, N., Barrón, V., and Torrent, J., 1999. Effect of phosphate on the crystallization of hematite, goethite, and lepidocrocite from ferrihydrite. *Clays Clay Min.* **47**, 304-311.

Gerke, J., 1993. Phosphate adsorption by humic/Fe-oxide mixtures aged at pH 4 and 7 and by poorly ordered Fe-oxide. *Geoderma* **59**, 279-288.

Griffioen, J., 2006. Extent of immobilisation of phosphate during aeration of nutrient-rich, anoxic groundwater. *Journal of Hydrology* **320**, 359-369.

Gunnars, A., Blomqvist, S., Johansson, P., and Andersson, C., 2002. Formation of Fe(III) oxyhydroxide colloids in freshwater and brackish seawater, with incorporation of phosphate and calcium. *Geochim. Cosmochim. Acta* **66**, 745-758.

Hsu, P. H., 1973. Complementary role of iron(III), sulfate and calcium in precipitation of phosphate from solution. *Environmental Letters* **5**, 115-136.

Hug, S. J. and Leupin, O., 2003. Iron-catalyzed oxidation of arsenic(III) by oxygen and by hydrogen peroxide: pH-dependent formation of oxidants in the Fenton reaction. *Environ. Sci. Technol.* **37**, 2734-2742.

Hug, S. J., Leupin, O. X., and Berg, M., 2009. Bangladesh and Vietnam: Different groundwater compositions require different approaches to arsenic mitigation. *Environ. Sci. Technol.* **42**, 6318-6323.

Jones, A. M., Collins, R. N., Rose, J., and Waite, T. D., 2009. The effect of silica and natural organic matter on the Fe(II)-catalysed transformation and reactivity of Fe(III) minerals. *Geochim. Cosmochim. Acta* **73**, 4409-4422.

Kaegi, R., Voegelin, A., Folini, D., and Hug, S. J., 2010. Effect of phosphate, silicate, and Ca on the morphology, structure and elemental composition of Fe(III)-precipitates formed in aerated Fe(II) and As(III) containing water. *Geochim. Cosmochim. Acta* **74**, 5798-5816.

Lienemann, C.-P., Monnerat, M., Dominik, J., and Perret, D., 1999. Identification of stoichiometric iron-phosphate colloids produced in a eutrophic lake. *Aquat. Sci.* **61**, 133-149.

Madrid, L. and De Arambarri, P., 1985. Adsorption of phosphate by two iron oxides in relation to their porosity. *Journal of Soil Science* **36**, 523-530.

Mao, Y., Pham, A. N., Rose, A. L., and Waite, T. D., 2011. Influence of phosphate on the oxidation kinetics of nanomolar Fe(II) in aqueous solution at circumneutral pH. *Geochim. Cosmochim. Acta* **75**, 4601-4610.

Mayer, D. T. and Jarrell, W. M., 2000. Phosphorus sorption during iron(II) oxidation in the presence of dissolved silica. *Water Research* **34**, 3949-3956.

McLaughlin, J. R. and Syers, J. K., 1978. Stability of ferric phosphates. *Journal of Soil Science* **29**, 499-504.

Meng, X. G., Korfiatis, G. P., Bang, S. B., and Bang, K. W., 2002. Combined effects of anions on arsenic removal by iron hydroxides. *Toxicol. Lett.* **133**, 103-111.

Miot, J., Benzerara, K., Morin, G., Kappler, A., Bernard, S., Obst, M., Férard, C., Skouri-Panet, F., Guigner, J.-M., Posth, N., Galvez, M., Brown, G. E., and Guyot, F., 2009. Iron biomineralization by anaerobic neutrophilic iron-oxidizing bacteria. *Geochim. Cosmochim. Acta* **73**, 696-711.

Moore, P. B. and Araki, T., 1977. Mitridatite, $Ca_6(H_2O)_6[FeIII_9O_6(PO_4)_9]\cdot 3H_2O$. A noteworthy octahedral sheet structure. *Am. Min.* **16**, 1096-1106.

Paktunc, D., Dutrizac, J., and Gertsman, V., 2008. Synthesis and phase transformations involving scorodite, ferric arsenate and arsenical ferrihydrite: Implications for arsenic mobility. *Geochim. Cosmochim. Acta* **72**, 2649-2672.

Pedersen, H. D., Postma, D., Jakobsen, R., and Larsen, O., 2005. Fast transformation of iron oxyhydroxides by the catalytic action of aqueous Fe(II). *Geochim. Cosmochim. Acta* **69**, 3967-3977.

Pokrovski, G. S., Schott, J., Farges, F., and Hazeman, J.-L., 2003. Iron(III)-silicate interactions in aqueous solution: Insights from X-ray absorption fine structure spectroscopy. *Geochim. Cosmochim. Acta* **67**, 3559-3573.

Pratesi, G., Cipriani, C., Giuli, G., and Birch, W. D., 2003. Santabarbaraite: a new amorphous phosphate mineral. *European Journal of Mineralogy* **15**, 185-192.

Ravel, B. and Newville, M., 2005. ATHENA, ARTEMIS, HEPHAESTUS: data analysis for X-ray absorption spectroscopy using IFEFFIT. *J. Synchrotron Rad.* **12**, 537-541.

Roberts, L. C., Hug, S. J., Dittmar, J., Voegelin, A., Saha, G. C., Ali, M. A., Badruzzaman, A. B. M., and Kretzschmar, R., 2007. Spatial distribution and temporal variability of arsenic in irrigated rice fields in Bangladesh: 1. Irrigation water. *Environ. Sci. Technol.* **41**, 5960-5966.

Roberts, L. C., Hug, S. J., Ruettimann, T., Billah, M. M., Khan, A. W., and Rahman, M. T., 2004. Arsenic removal with iron(II) and iron(III) in waters with high silicate and phosphate concentrations. *Environ. Sci. Technol.* **38**, 307-315.

Rose, J., Manceau, A., Bottero, J. Y., Masion, A., and Garcia, F., 1996. Nucleation and growth mechanisms of Fe oxyhydroxide in the presence of PO_4 ions. 1. Fe K-edge EXAFS study. *Langmuir* **12**, 6701-6707.

Schwertmann, U. and Taylor, R. M., 1979. Natural and synthetic poorly crystallized lepidocrocite. *Clay Minerals* **14**, 285-293.

Stumm, W. and Sigg, L., 1979. Kolloidchemische Grundlagen der Phosphor-Elimination in Fällung, Flockung und Filtration. *Zeitschrift für Wasser- und Abwasser-Forschung* **12**, 73-83.

Tamura, H., Goto, K., and Nagayama, M., 1976. Effect of anions on the oxygenation of ferrous ion in neutral solutions. *Journal of Inorganic and Nuclear Chemistry* **38**, 113-117.

Tamura, H., Kawamura, S., and Hagayama, M., 1980. Acceleration of the oxidation of Fe^{2+} ions by Fe(III)-oxyhydroxides. *Corrosion Science* **20**, 963-971.

Tessenow, U., 1974. Lösungs-, Diffusions- und Sorptionsprozesse in der Oberschicht von Seesedimenten. IV. Reaktionsmechanismen und Gleichgewichte im System Eisen-Mangan-Phosphat im Hinblick auf die Vivianitakkumulation im Ursee. *Arch. Hydrobiol. Suppl.* **47**, 1-79.

Thibault, P.-J., Rancourt, D. G., Evans, R. J., and Dutrizac, J., 2009. Mineralogical confirmation of a near-P:Fe = 1:2 limiting stoichiometric ratio in colloidal P-bearing ferrihydrite-like hydrous ferric oxide. *Geochim. Cosmochim. Acta* **73**, 364-376.

Venema, P., Hiemstra, T., and van Riemsdijk, W. H., 1997. Interaction of cadmium with phosphate on goethite. *J. Colloid Interface Sci.* **192**, 94-103.

Voegelin, A., Kaegi, R., Frommer, J., Vantelon, D., and Hug, S. J., 2010. Effect of phosphate, silicate, and Ca on Fe(III)-precipitates formed in aerated Fe(II)- and As(III)-containing water studied by X-ray absorption spectroscopy. *Geochim. Cosmochim. Acta* **74**, 164-186.

Voegelin, A., Weber, F.-A., and Kretzschmar, R., 2007. Distribution and speciation of arsenic around roots in a contaminated riparian floodplain soil: Micro-XRF element mapping and EXAFS spectroscopy. *Geochim. Cosmochim. Acta* **71**, 5804-5820.

Williams, A. G. B. and Scherer, M. M., 2004. Spectroscopic evidence for Fe(II)-Fe(III) electron transfer at the iron oxide-water interface. *Environ. Sci. Technol.* **38**, 4782-4790.

Williams, D. B. and Carter, C. B., 2009. *Transmission Electron Microscopy. A Textbook for Materials Science*. Springer, New York.

Wolthoorn, A., Temminghoff, E. J. M., Weng, L. P., and van Riemsdijk, W. H., 2004. Colloid formation in groundwater: effect of phosphate, manganese, silicate and dissolved organic matter on the dynamic heterogeneous oxidation of ferrous iron. *Appl. Geochem.* **19**, 611-622.

6. TABLES

Table 1. Chemical parameters and Fe K-edge EXAFS LCF results for P/Fe series at pH 7.0. LCF results are displayed in Fig. 1b, and LCF spectra in Fig. 3 and Fig. EA5.

	Chemical parameters [a]			LCF results [b]					
Sample name	$Fe(II)_{(t=0)}$ (mM)	$(P/Fe)_{soln}$ (—)	$(P/Fe)_{ppt}$ (—)	Fe-P (—)	HFO (—)	Goe (—)	Lp (—)	Sum (—)	NSSR (×1000)
P/Fe 0.00	1.00	0.000	0.000	—	0.25	0.17	0.58	1.06	4.5
[c] P/Fe 0.00b	0.54	0.000	0.000	—	0.19	0.13	0.68	1.02	2.3
[d] P/Fe 0.00c	1.11	0.000	0.000	—	0.35	0.09	0.56	1.08	2.3
P/Fe 0.03	1.00	0.025	0.026	—	0.43	—	0.57	1.08	4.1
P/Fe 0.06	1.00	0.057	0.057	—	0.50	0.04	0.46	1.07	3.3
P/Fe 0.09	1.00	0.087	0.084	—	0.58	0.04	0.38	1.08	3.8
P/Fe 0.12	1.00	0.116	0.115	—	0.59	0.05	0.37	1.09	3.1
[c] P/Fe 0.12b	0.54	0.120	0.106	—	0.47	0.04	0.49	1.05	1.9
P/Fe 0.14	1.00	0.142	0.134	—	0.67	—	0.33	1.09	4.0
P/Fe 0.19	1.00	0.194	0.186	0.11	0.60	—	0.29	1.07	3.7
P/Fe 0.25	1.00	0.246	0.245	0.30	0.44	—	0.26	1.04	5.3
P/Fe 0.29	1.00	0.289	0.281	0.24	0.59	—	0.17	1.07	2.7
P/Fe 0.38	1.01	0.378	0.371	0.36	0.54	—	0.10	1.06	4.6
[c] P/Fe 0.42b	0.54	0.420	0.391	0.50	0.43	—	0.07	0.98	2.0
P/Fe 0.50	1.00	0.497	0.501	0.93	—	—	0.07	0.97	5.9
P/Fe 0.55	1.04	0.553	0.530	1.00	—	—	—	0.94	6.0
[d] P/Fe 0.58c	1.07	0.575	0.562	1.00	—	—	—	0.97	5.2
P/Fe 0.70	1.06	0.704	0.602	1.00	—	—	—	0.97	7.5
P/Fe 0.95	1.00	0.954	0.629	1.00	—	—	—	1.01	7.3
[c] P/Fe 1.20b	0.54	1.201	0.594	1.00	—	—	—	0.91	5.8
P/Fe 1.40	1.00	1.402	0.674	1.00	—	—	—	0.98	6.5
P/Fe 1.91	0.99	1.909	0.718	1.00	—	—	—	0.99	6.4

[a] Spiked concentration of Fe(II), initial molar dissolved P/Fe ratio, and molar P/Fe ratio of precipitate.

[b] EXAFS LCF analysis over k-range 2-11 $Å^{-1}$ using reference spectra of amorphous Fe(III)-phosphate (Fe-P), hydrous ferric oxide (HFO), goethite (Goe), and lepidocrocite (Lp) (Fig. 3) from Voegelin et al. (2010). Fractions normalized to a sum of 1.00 are reported together with the effective (non-constrained) sum of all fitted fractions. Statistical fit uncertainties were typically <0.015, but reached up to 0.040 for Fe-P and HFO in fits including both spectra. NSSR: normalized sum of squared residuals ($NSSR = \sum(data_i - fit_i)^2/\sum(data_i)^2$).

[c] Samples from Voegelin et al. (2010) synthesized at a total Fe concentration of 0.54 mM (in 8 mM $NaHCO_3$ at pH 7.0).

[d] Initial precipitates from precipitate mixing experiment.

Table 2. Chemical parameters and Fe K-edge EXAFS LCF results for samples from the time-resolved Fe(II) oxidation experiment (Fig. 6).

	Chemical data [a]		**LCF results** [b]					
Sample name	Fe (mM)	$(P/Fe)_{ppt}$ (—)	Fe-P (—)	HFO (—)	Goe (—)	Lp (—)	Sum (—)	NSSR (x1000)
p-0-60	0.57	0.52	1.00	—	—	—	0.98	5.7
p-60-300	0.43	0.00	—	0.31	0.13	0.56	1.07	7.2
p-0-300	1.00	0.29	0.34	0.44	—	0.21	1.06	2.0
			Calculated [c]					
#c-0-300			0.55	0.14	0.06	0.25	1.02	
&c-60-300			-0.40	0.95	—	0.45	1.16	

[a] Amount of precipitated Fe (initial Fe(II) spike: 1.00 mM) and molar P/Fe ratio of precipitate.
[b] Fractions normalized to a sum of 1.00 are reported together with the effective (non-constrained) sum of all fitted fractions. For further details see footnote be of Table 1.
[c] Calculated Fe fractions were derived from LCF results by taking the amounts of Fe into account. "c-0-300": Final precipitate composition in case of sequential precipitation of p-0-60 followed by p-60-300 calculated as 0.57×"p-0-60" + 0.43×"p-60-300". "c-60-300": Structural change induced by Fe(II) oxidation from 60 to 300 min calculated as ("p-0-300"-0.57×"p-0-60")/0.43.

Table 3. LCF results for difference spectra from mixing and sequential Fe(II) addition experiments. LCF results are shown in Fig. 7 (experimental, difference and LCF spectra in Fig. EA9).

	Calculation [a]	LCF results [b]					
		Fe-P	HFO	Goe	Lp	Sum	NSSR
Spectrum	A	(—)	(—)	(—)	(—)	(—)	(x1000)
[c] P/Fe 0.00c	—	—	0.35	0.09	0.56	1.08	2.3
d-Mix 0.30	0.50	—	0.35	0.09	0.56	1.07	3.9
d-Mix 0.15	0.25	—	0.31	0.10	0.59	1.06	3.0
d-Seq 0.30	0.50	-0.17	0.65	0.03	0.49	1.09	5.9
d-Seq 0.15	0.25	-0.20	0.67	0.03	0.50	1.12	4.3

[a] Difference spectra were calculated from normalized XAS spectra as ”d-spectrum” = ”spectrum”-A×”P/Fe 0.58c”

[b] Fractions normalized to a sum of 1.00 are reported together with the effective (non-constrained) sum of all fitted fractions. Statistical fit uncertainties were typically <0.015, but were 0.039/0.035 for Fe-P and 0.055/0.049 for HFO in fits of d-Seq 0.30/d-Seq 0.15 including both spectra. For further details on LCF fits see footnote b of Table 1.

[c] LCF results for sample P/Fe 0.00c formed in absence of P shown for direct comparison.

7. FIGURES

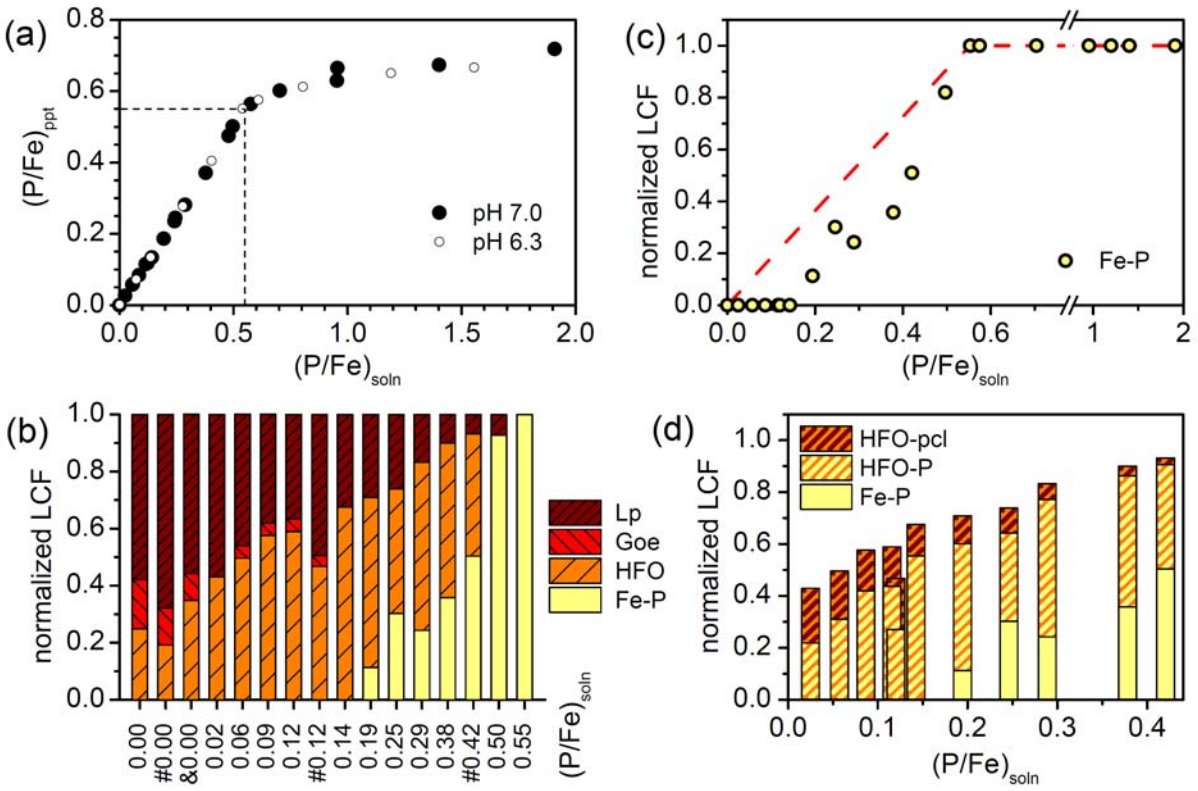

Fig. 1. (a) Molar P/Fe ratios of Fe(III)-precipitates versus initial dissolved molar P/Fe (8 mM $NaHCO_3$; 1 mM Fe(II), initial pH 7.0 or 6.3). Dashed vertical and horizontal lines represent $(P/Fe)_{soln}$ and $(P/Fe)_{ppt}$ of 0.55, respectively. (b) EXAFS LCF results for P/Fe series at pH 7.0. All precipitates at $(P/Fe)_{soln} \geq 0.55$ were fit as 100% Fe-P. [#]Precipitates synthesized at 0.54 mM total Fe from Voegelin et al. (2010). [&]Sample from mixing experiment. Complete LCF results are provided in Table 1, selected spectra are shown in Fig. 3. (c) LCF-derived Fe(III)-phosphate fraction versus initial dissolved P/Fe. Dashed red line indicates expected Fe-P fraction if formation of Fe(III)-phosphate with P/Fe 0.55 was followed by formation of phosphate-free Fe(III)-(hydr)oxides. (d) Fractions of Fe-phosphate (Fe-P), phosphate-related HFO (HFO-P), and HFO related to poorly crystalline lepidocrocite/goethite (HFO-pcl). HFO-pcl was calculated from the sum of the LCF-derived Lp and Goe fractions based on the average HFO/(Lp+Goe) ratio of the 3 phosphate-free Fe(III)-precipitates (0.37). HFO-P was obtained by subtracting HFO-pcl from the fitted HFO fraction.

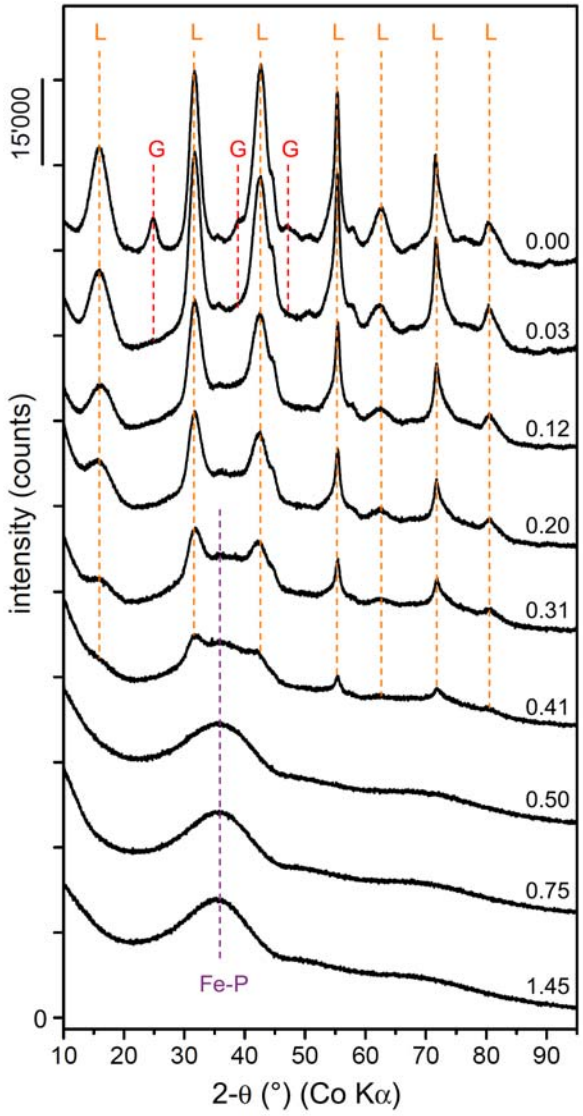

Fig. 2. X-ray diffraction patterns of Fe(III)-precipitates formed at initial dissolved molar P/Fe ratios from 0.00 to 1.45 (8 mM $NaHCO_3$; 1 mM Fe(II), initial pH 7.0). Numbers at right of each diffractogram indicate the molar initial dissolved P/Fe ratios during synthesis. Dashed vertical lines indicate dominant peaks of lepidocrocite (L), goethite (G), and amorphous Fe(III)-phosphate (Fe-P). Patterns are offset by 15'000 counts. Note: Precipitates for XRD analysis were synthesized separately in larger solution volumes and are not identical to the samples evaluated by XAS and TEM.

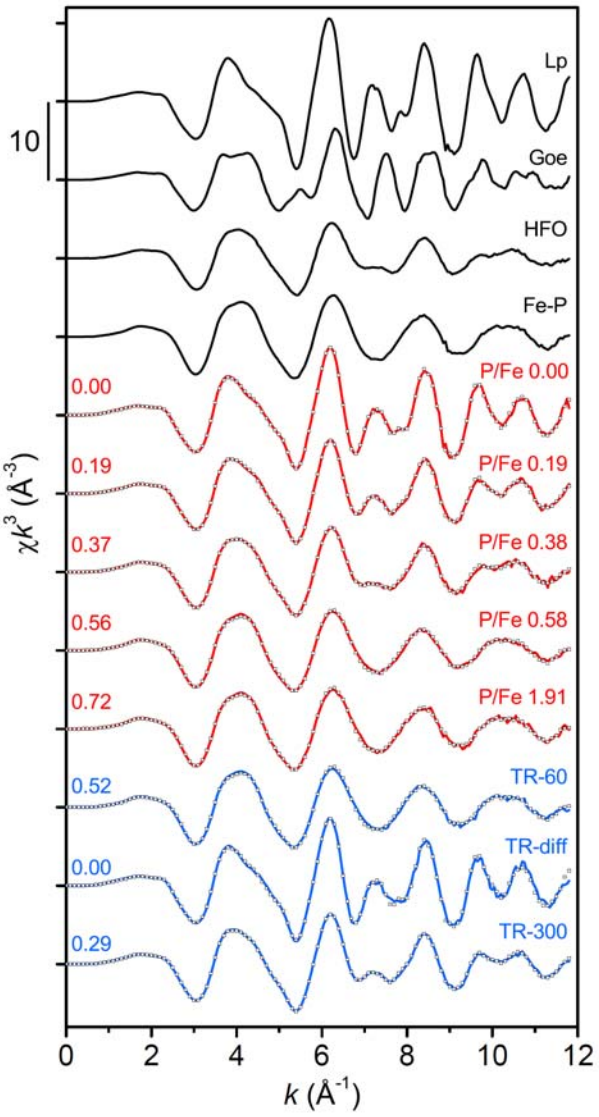

1

2 Fig. 3. Fe K-edge EXAFS spectra of reference materials (from Voegelin et al. (2010)), of
3 selected samples from P/Fe series at pH 7.0 (Fig. 1; all sample spectra in Fig. EA5, sample
4 details and LCF results in Table 1), of samples from time-resolved experiment (Fig. 6; sample
5 details and LCF results in Table 2) (lines) and of LCF spectra (open squares; LCF results
6 provided in Table 1). Numbers at the left of each sample spectrum indicate the molar P/Fe ratio
7 of the precipitates.

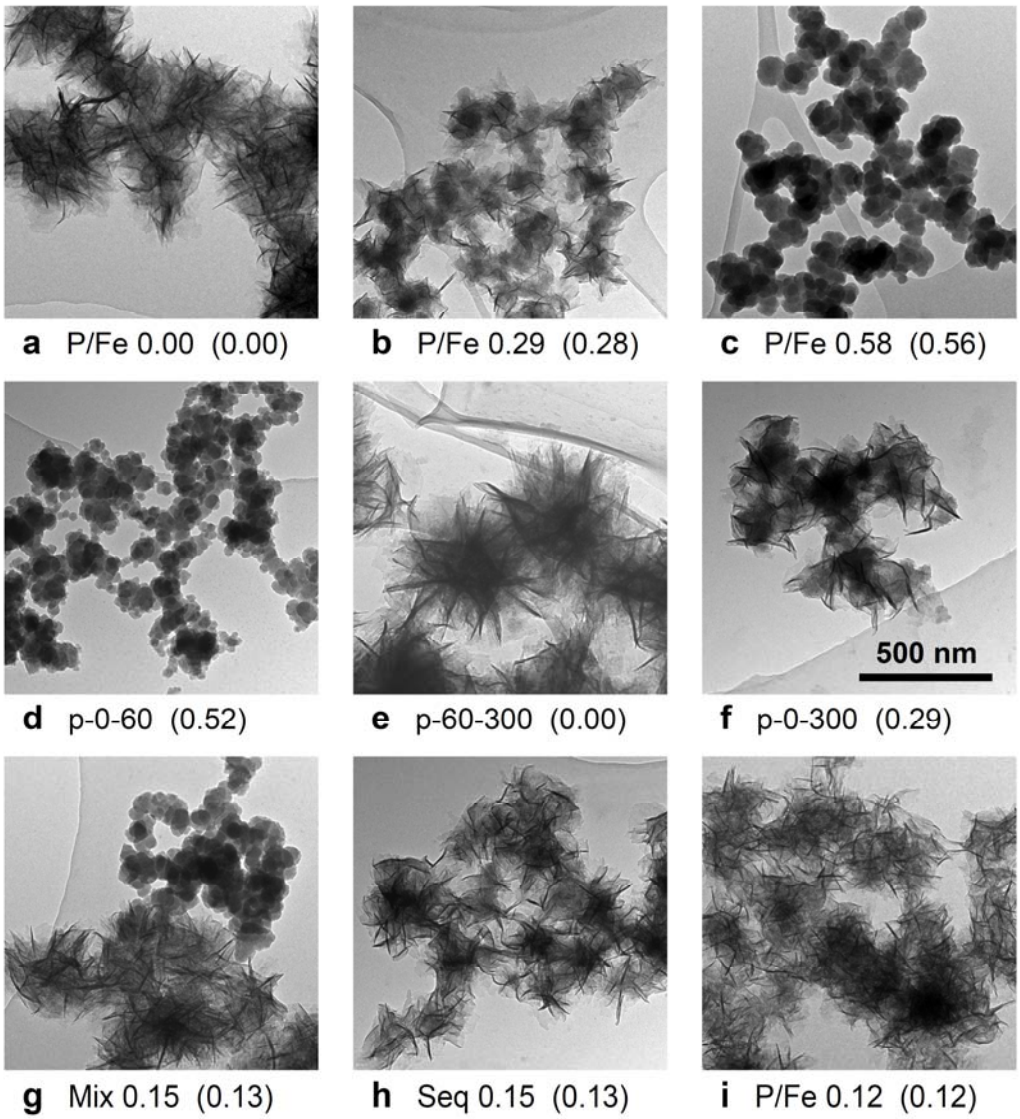

Fig. 4. Bright field TEM images of Fe(II) oxidation products. (a,b,c,i) Precipitates from P/Fe series (Fig. 1, Table 1). (d,e,f) Precipitates from time-resolved experiment (Fig. 6, Table 2). (g,h,i) Precipitates from mixing and sequence experiment (at nominal total P/Fe of 0.15) compared to precipitate from P/Fe series with similar molar P/Fe ratio. Numbers in parentheses indicate the molar P/Fe ratios of the precipitates. Scale bar in panel f applies to all panels.

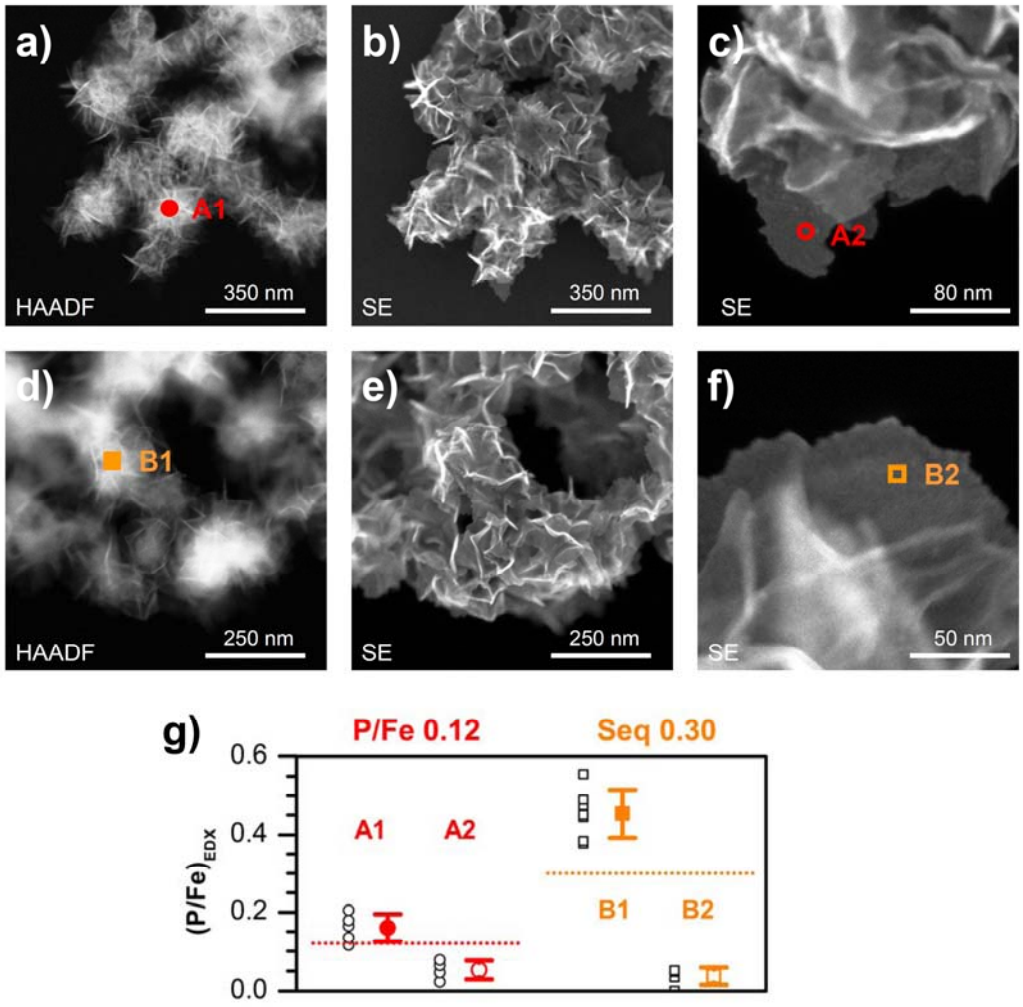

Fig. 5. High-angle annular dark-field (HAADF) and secondary electron (SE) STEM images of (a.b.c) precipitate P/Fe 0.12 from P/Fe series and (d,e,f,) precipitate Seq 0.30 from sequential Fe(II) addition experiment. EDX spectra were recorded on locations of type A1/B1 (dense zones visible in HAADF images) and A2/B2 (isolated lepidocrocite platelets). (g) Molar P/Fe ratios from EDX analyses on locations of type A1 (n=5) and A2 (n=4) on sample P/Fe 0.12 and B1 (n=7) and B2 (n=5) on sample Seq 0.30. Open black squares and circles represent individual data points, colored symbols with error bars represent average and standard deviation. Horizontal dotted lines indicate the bulk P/Fe ratio of the precipitates.

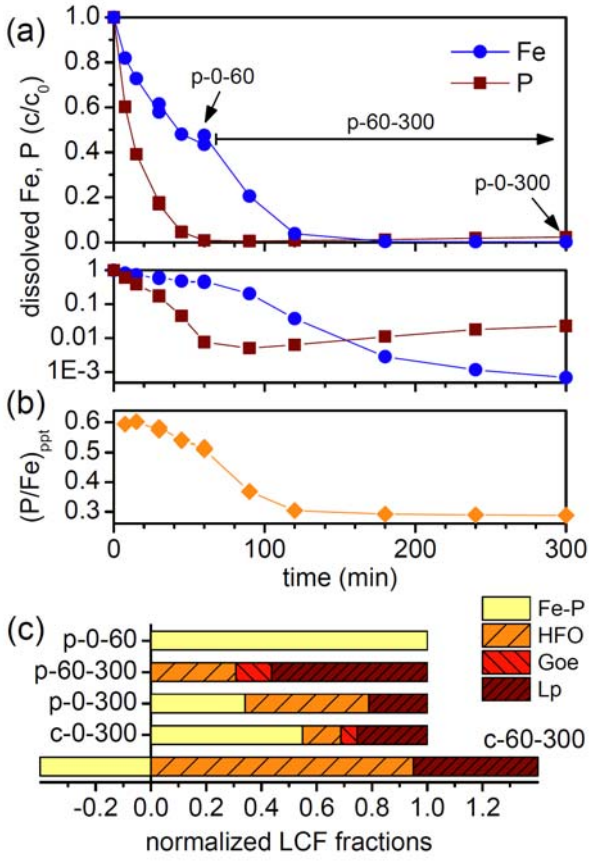

Fig. 6. (a) Dissolved Fe and P (<0.2 µm) fraction during oxidation of 1 mM Fe(II) at a molar initial dissolved P/Fe ratio of 0.3 in 8 mM $NaHCO_3$ at initial pH 6.3 (on linear and logarithmic scale). Labels with arrows indicate samples studied by XAS and TEM. (b) Change in molar precipitate P/Fe ratio over time. The comparison with a replicate experiment is shown in Fig. EA6. (c) Results from LCF analysis of the Fe precipitates "p-0-60" (after 60 min), "p-0-300" (after 300 min), and "p-60-300" (formed in filtrate collected after 60 min). Corresponding EXAFS spectra are shown in Fig. 3, complete LCF results are listed in Table 2. "c-0-300" was calculated from the LCF results for samples p-0-60 and p-60-300 weighed by the respective amounts of Fe. It represents the speciation expected after 300 min if continuing Fe(II) oxidation from 60 to 300 min did not affect already precipitated Fe. "c-60-300" was calculated from the LCF results for samples p-0-60 and p-0-300 and represents the Fe speciation change induced by Fe(II) oxidation and precipitate aging from 60 to 300 min.

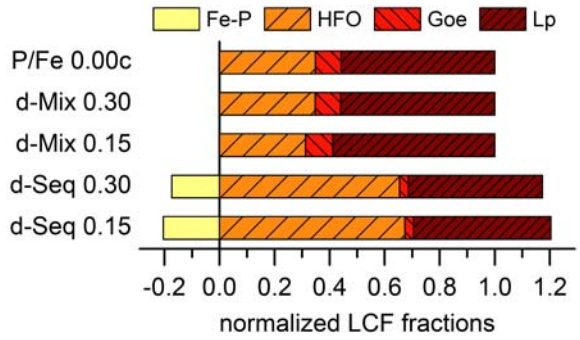

1

2 Fig. 7. LCF analysis of difference spectra from the mixing (Mix) and sequential Fe(II) addition
3 (Seq) experiments. Further details are provided in section 3.3 and Table 3.

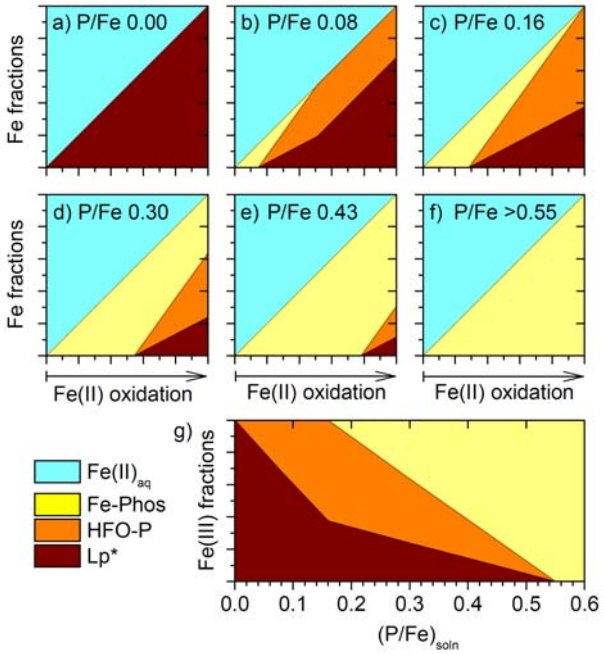

Fig. 8. Conceptual model. (a-f) Fe species evolution from 0 to 100% Fe(II) oxidation at different molar initial dissolved P/Fe ratios and (g) Fe(III)-precipitate speciation after complete Fe(II) oxidation as a function of initial P/Fe ratio considering the species "$Fe(II)_{aq}$" (dissolved Fe(II)), "Fe-Phos" (Fe(III)-phosphate with P/Fe of 0.55), "HFO-P" (HFO with P/Fe of 0.25) and "Lp*" (lepidocrocite, goethite (at P/Fe = 0) and HFO-pcl related to poorly crystalline lepidocrocite). Calculations are based on the following sequence: (i) Fe-Phos formation until dissolved phosphate depletion, (ii) transformation of Fe-Phos into HFO-P and parallel formation of 0.59 Lp* per HFO-P, and (iii) exclusive Lp* formation after complete Fe-Phos transformation to HFO-P.

Electronic Annex to GCA manuscript

Dynamic Fe-precipitate formation induced by Fe(II) oxidation in aerated phosphate-containing water

Andreas Voegelin[a*], Anna C. Senn[a], Ralf Kaegi[a], Stephan J. Hug[a], Stefan Mangold[b]

[a] Eawag, Swiss Federal Institute of Aquatic Science and Technology, Ueberlandstrasse 133, CH-8600 Duebendorf, Switzerland.

[b] Karlsruhe Institute of Technology, Institute of Synchrotron Radiation, Hermann-von-Helmholtz-Platz 1, D-76344 Eggenstein-Leopoldshafen, Germany.

[*] Corresponding author. E-mail address: andreas.voegelin@eawag.ch, phone +41 58 765 54 70

CONTENT (9 pages, 1 table, 9 figures)

1. P/Fe series

1.1. Pictures

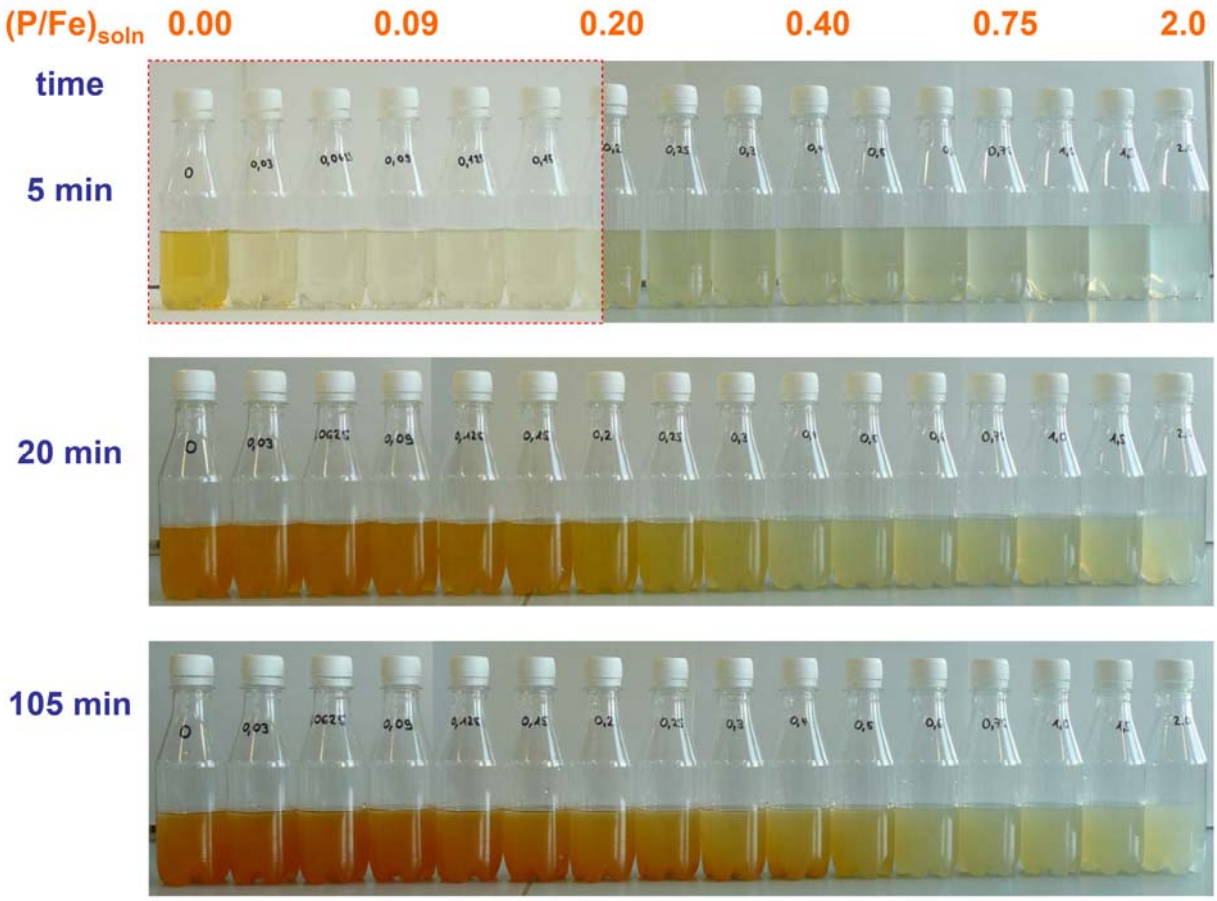

Fig. EA1. Pictures of precipitate suspensions at P/Fe ratios from 0 to 2 at increasing times after Fe(II) addition. Pictures were taken from precipitates synthesized at pH 7.0 (used for XAS and TEM), except for precipitates at P/Fe up to 0.2 after 5 min, which were synthesized separately at slightly lower pH 6.9 (marked with red dashed line; direct comparison of the two images for precipitate at P/Fe 0.2 indicates effect of different illumination). No further color changes were observed from 105 min until sample collection (300 min). Final suspensions exhibit a color transition from orange at very low P/Fe ratios (reflecting dominant lepidocrocite formation) to beige at P/Fe ratios >0.5 (reflecting formation of amorphous Fe(III)-phosphate). Suspension colors 5 minutes after Fe(II) addition reveal initial Fe(III)-phosphate formation down to the lowest tested P/Fe ratio of 0.03.

1.2. Lepidocrocite: fractions from XRD and XAS and XRD peak width

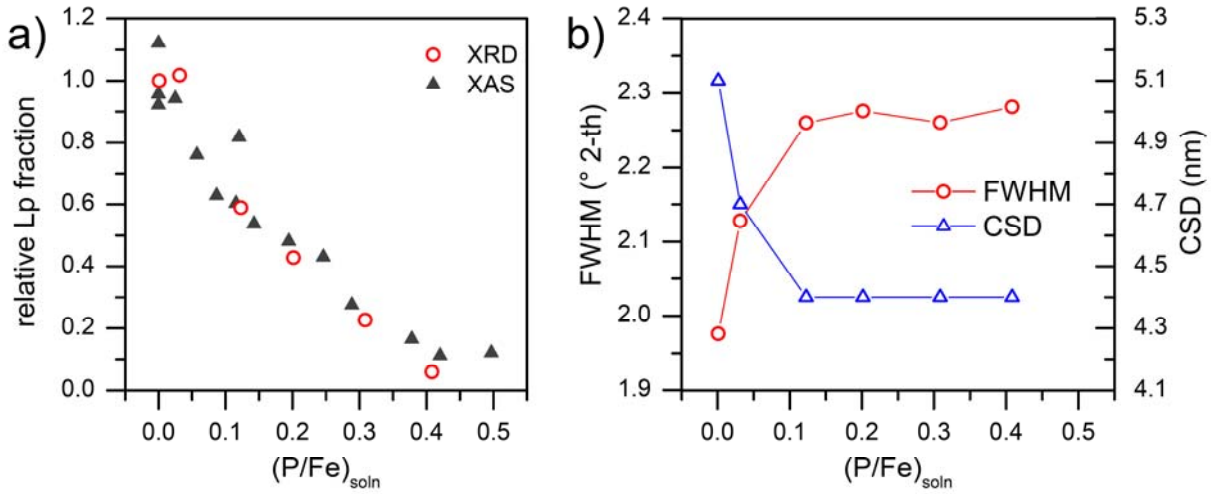

Fig. EA2. (a) Fraction of lepidocrocite relative to phosphate-free Fe(III)-precipitate as a function of $(P/Fe)_{soln}$ as derived from XRD (relative area of 301 peak at 31.7° 2-θ) and LCF analysis (Table 1). (b) Full width at half maximum (FWHM) of the 301 peak of lepidocrocite as a function of $(P/Fe)_{soln}$ and corresponding coherently scattering domain (CSD) size (estimated with Scherrer equation (shape-factor K=0.9).

1.3. Measured and calculated dry precipitate mass

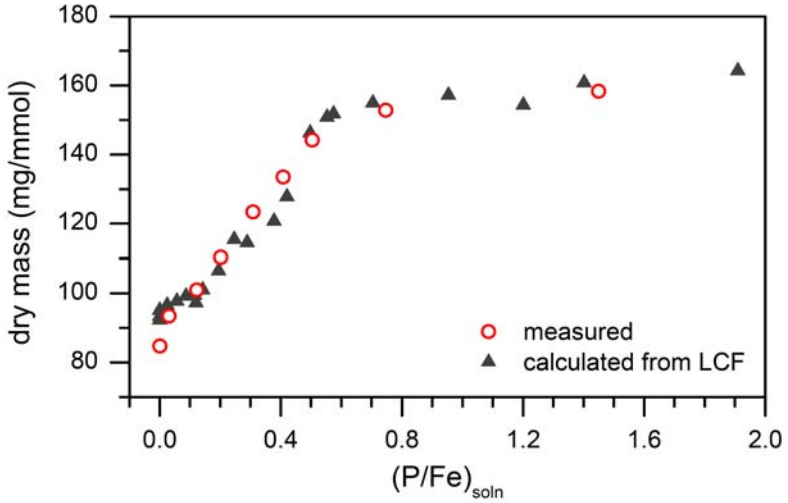

Fig. EA3. Measured dry mass of precipitates analyzed by XRD (Fig. 2) and FTIR (Fig. EA4) and calculated dry mass of precipitates analyzed by XAS based on LCF results (expressed per mmol Fe) as a function of molar initial dissolved P/Fe ratio. For the LCF-based calculation the molar masses of the individual phases were multiplied with the respective LCF fractions (Table 1) and summed up. The molar mass of Lp and Goe (FeOOH) is 88.85 mg/mmol. For HFO, a molar mass of 107 mg/mmol was assumed ($Fe(OH)_3$). For the molar mass of the Fe(III)-phosphate fraction, we assumed a stoichiometry $[FePO_4{\times}2H_2O]_x[Fe(OH)_3]_{(1-x)}$ with x set to 0.55 for precipitates formed at initial dissolved P/Fe ratios <0.55 and to the $(P/Fe)_{ppt}$ ratio determined by ICP-MS (Table 1) for precipitates formed at initial dissolved P/Fe ratios >0.55.

1.4. FTIR spectra

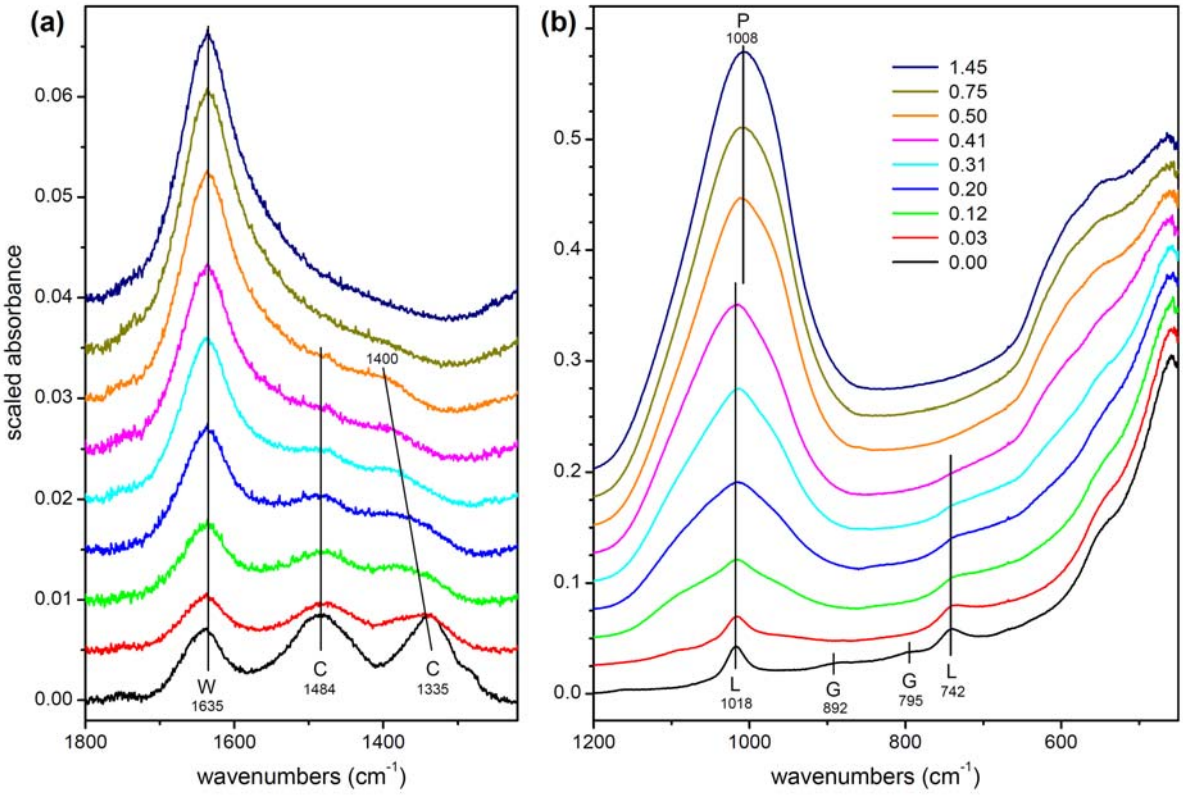

Fig. EA4. Fourier-transform infrared spectra of precipitates formed at pH 7.0 at initial dissolved P/Fe ratios from 0.00 to 1.45. The spectra were scaled to the average absorbance of all spectra in the wavenumbers range 455-465 cm^{-1} and set to an average absorbance of zero in the ranges 1225-1235 and 1790-1800 cm^{-1} by subtracting a linear baseline between those points. For clarity, spectra were offset by 0.005 absorbance units in panel a and by 0.02 absorbance units in panel b. Bands at 742 and 1018 cm^{-1} are characteristic for lepidocrocite (L) with platy morphology, and bands at 795 and 892 cm^{-1} for goethite (G) *(Cornell and Schwertmann, 2003)*. Goethite bands are only visible in the precipitate formed in the absence of phosphate, whereas lepidocrocite bands (especially at 742 cm^{-1}) can be seen up to an initial dissolved P/Fe ratio of 0.31. The band at 1008 cm^{-1} reflects the increasing phosphate content of the precipitates with increasing initial dissolved P/Fe. The carbonate bands of the phosphate-free precipitate at 1335 and 1484 cm^{-1} (C) agree closely with reported positions for carbonate adsorbed on goethite at pH 7.2-9.2 *(Villalobos and Leckie, 2001)*. The suppression of goethite formation at a P/Fe ratio of 0.03 (as also observed by XRD, Fig. 2) is probably related to the drastic decrease in carbonate uptake in the presence of phosphate, considering that carbonate favors goethite over lepidocrocite formation (Carlson and Schwertmann, 1990). Further decreasing amounts of carbonate are detected up to a P/Fe ratio of 0.50, possibly related to the residual lepidocrocite fraction. The band at 1635 cm^{-1} arises from surface bound or structural water (W). Its pronounced increase from P/Fe 0.12 to 0.75 may be attributed to the increasing fraction of hydrated amorphous Fe(III)-phosphate in the precipitate.

1.5. Fe K-edge EXAFS spectra

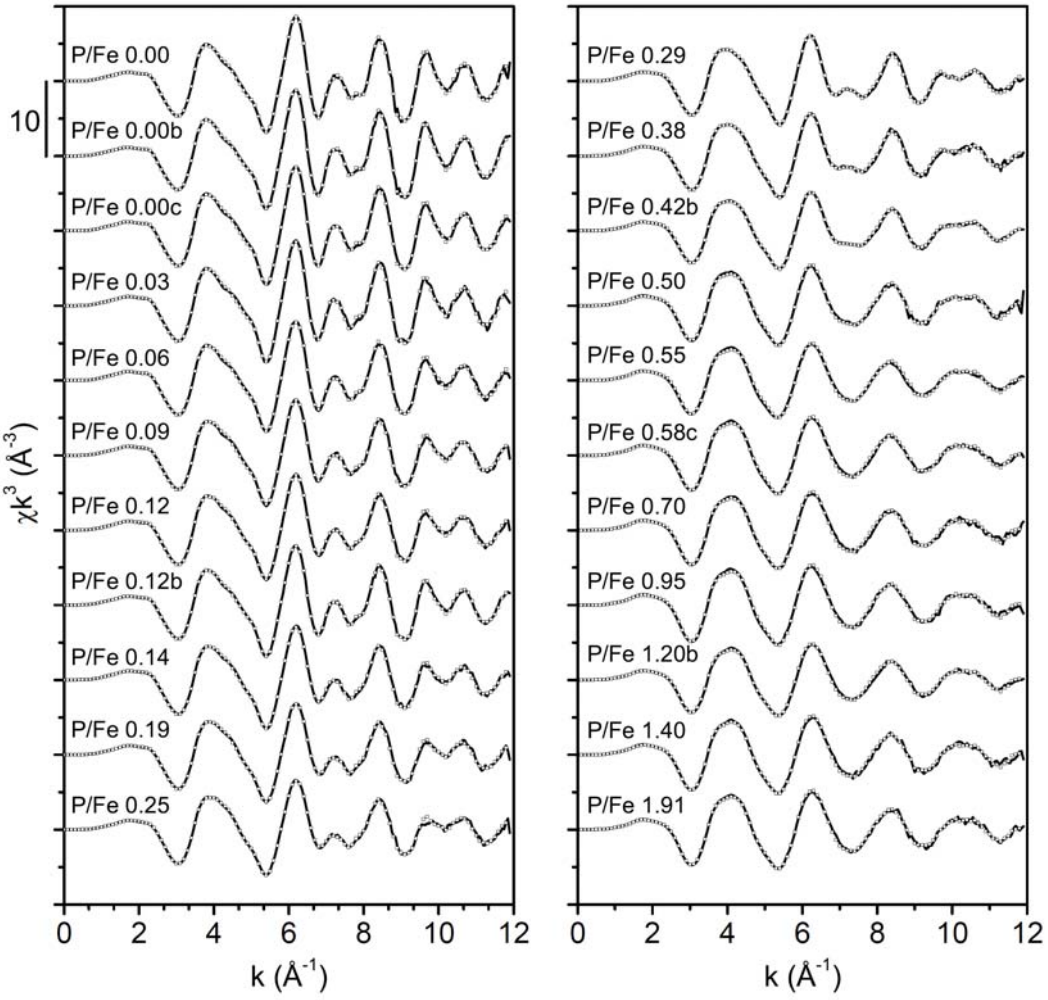

Fig. EA5. Fe K-edge EXAFS spectra of precipitates from the P/Fe series at pH 7.0 in 8 mM $NaHCO_3$ arranged from top left to bottom right along increasing molar P/Fe ratio in solution (solid lines) and LCF spectra (open squares). Sample details and LCF results listed in Table 1.

1.6. Calculation of HFO-P and $(P/Fe)_{HFO-P}$ ratio

Table EA1. (A) Differentiation of LCF-derived HFO fraction into HFO related to poorly crystalline lepidocrocite and goethite (HFO-pcl) and phosphate-rich HFO (HFO-P): The average ratio HFO/(Lp+Goe) of the 3 phosphate-free precipitates was assumed to correspond to the ratio HFO-pcl/(Lp+Goe) of phosphate-containing precipitates and was used to calculate HFO-pcl from the LCF-derived Lp+Goe fractions. HFO-P was obtained by subtracting HFO-pcl from HFO. **(B)** Calculation of molar (P/Fe) ratios of HFO-P and HFO: First, the LCF-derived Fe(III)-phosphate fraction (Fe-P) was multiplied by the characteristic $(P/Fe)_{Fe-P}$ ratio of 0.55. The result was subtracted from the experimentally determined $(P/Fe)_{ppt}$ to obtain the residual (P/Fe) not originating from Fe-P. This residual P/Fe ratio was divided by the fraction of HFO-P or HFO of each sample to obtain the molar $(P/Fe)_{HFO-P}$ and $(P/Fe)_{HFO}$ ratios, respectively. The average $(P/Fe)_{HFO-P}$ was calculated from all phosphate-containing samples for which LCF returned an HFO fraction (n=11). The calculation of the average $(P/Fe)_{HFO}$ was limited to the samples with precipitate P/Fe ratios ≥0.14 (where HFO-P accounted for most of the HFO and HFO was assumed to be nearly saturated with phosphate; n=6). Based on the LCF-derived fractions of Fe-P and HFO-P and $(P/Fe)_{Fe-P}$ and $(P/Fe)_{HFO-P}$ ratios of 0.55 and 0.25, the P/Fe ratios of individual precipitates were calculated ($(P/Fe)_{ppt,calc}$). Comparison with experimentally determined ratios ($(P/Fe)_{ppt}$) indicated a close correlation (r=0.986).

Sample	Experimental (P/Fe)		LCF results				Differentiation of HFO	
	$(P/Fe)_{soln}$	$(P/Fe)_{ppt}$	Fe-P	HFO	Goe	Lp	HFO/(Lp+Goe)	
P/Fe 0.00	0.00	0.00		0.25	0.17	0.58	0.33	
P/Fe 0.00b	0.00	0.00		0.19	0.13	0.68	0.24	
P/Fe 0.00c	0.00	0.00		0.35	0.09	0.56	0.53	
							0.37	average
							0.15	s.d. (n=3)
	$(P/Fe)_{soln}$	$(P/Fe)_{ppt}$	Fe-P	HFO	Goe	Lp	**HFO-pcl**	**HFO-P**
P/Fe 0.03	0.02	0.03		0.43		0.57	0.21	0.22
P/Fe 0.06	0.06	0.06		0.50	0.04	0.46	0.18	0.31
P/Fe 0.09	0.09	0.08		0.58	0.04	0.38	0.16	0.42
P/Fe 0.12	0.12	0.11		0.59	0.05	0.37	0.15	0.44
P/Fe 0.12b	0.12	0.11		0.47	0.04	0.49	0.20	0.27
P/Fe 0.14	0.14	0.13		0.67		0.33	0.12	0.56
P/Fe 0.19	0.19	0.19	0.11	0.60		0.29	0.11	0.49
P/Fe 0.25	0.25	0.24	0.30	0.44		0.26	0.10	0.34
P/Fe 0.29	0.29	0.28	0.24	0.59		0.17	0.06	0.53
P/Fe 0.38	0.38	0.37	0.36	0.54		0.10	0.04	0.51
P/Fe 0.42b	0.42	0.39	0.50	0.43		0.07	0.03	0.40

P/Fe ratios of HFO-P and HFO		
	$(P/Fe)_{HFO-P}$	**$(P/Fe)_{HFO}$**
average	0.25	0.24
s.d.	0.07	0.05
n	11	6

$(P/Fe)_{Fe-P}$=0.55

	$(P/Fe)_{ppt}$ from Fe-P	residual $(P/Fe)_{ppt}$	$(P/Fe)_{HFO-P}$	$(P/Fe)_{HFO}$	$(P/Fe)_{ppt,clc}$
P/Fe 0.03	0.00	0.03	0.12	*0.06*	0.06
P/Fe 0.06	0.00	0.06	0.18	*0.12*	0.08
P/Fe 0.09	0.00	0.08	0.20	*0.15*	0.11
P/Fe 0.12	0.00	0.11	0.26	*0.20*	0.11
P/Fe 0.12b	0.00	0.11	0.39	*0.23*	0.07
P/Fe 0.14	0.00	0.13	0.24	0.20	0.14
P/Fe 0.19	0.06	0.12	0.25	0.21	0.19
P/Fe 0.25	0.17	0.08	0.23	0.18	0.25
P/Fe 0.29	0.13	0.15	0.28	0.25	0.27
P/Fe 0.38	0.20	0.17	0.34	0.32	0.32
P/Fe 0.42b	0.28	0.11	0.28	0.27	0.38

2. Time-resolved experiment: Replicate experiment, UV-Vis analyses, and pictures

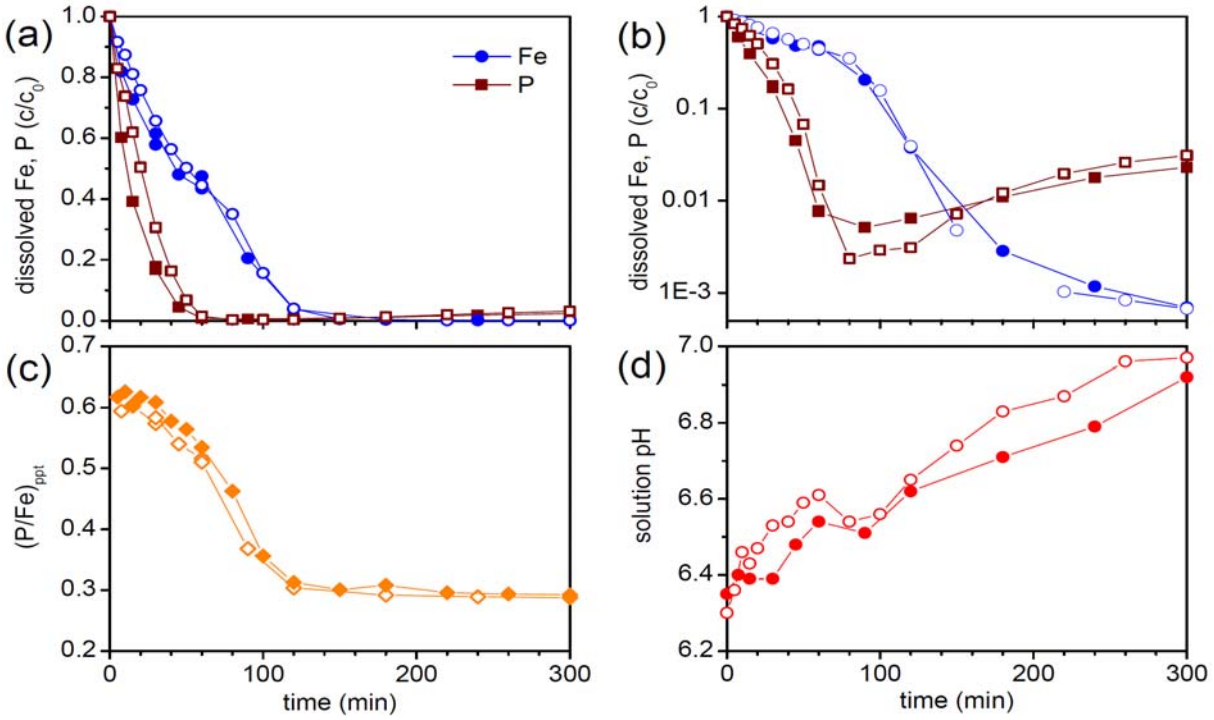

Fig. EA6. Comparison of time-resolved experiment with one replicate. (a,b) Dissolved Fe and P fractions (from ICP-MS) on linear and logarithmic scale, (c) precipitate P/Fe ratio, and (d) solution pH. Solid symbols refer to experiment in manuscript from which solids for XAS and TEM were collected. Open symbols represent replicate experiment used for the UV-Vis spectrometric determination of Fe(II) and Fe_{tot} in unfiltered and filtered solutions (Fig. EA7).

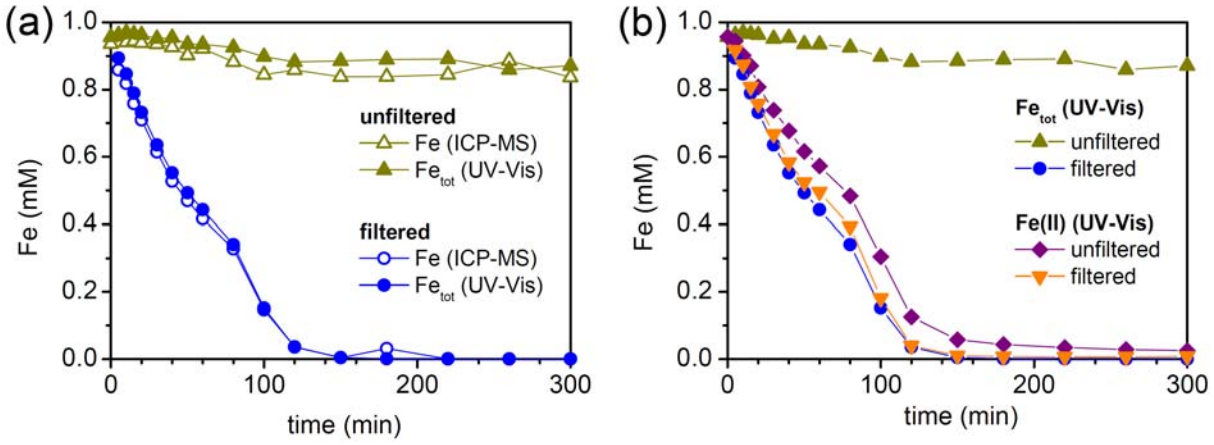

Fig. EA7. (a) Total Fe measured by ICP-MS and UV-Vis in unfiltered and filtered (0.2 µm) suspensions. (b) Total Fe and Fe(II) measured by UV-Vis in unfiltered and filtered suspensions.

In Fig. EA6, results from a replicate experiment are compared to corresponding data from the experiment reported in Fig. 6 in the manuscript. Precipitates for analysis by XAS and TEM were collected from the experiment reported in Fig. 6. The comparison indicates the degree of reproducibility. During the experiments, the pH increased from initially ~6.3 to ~6.9, due to loss of CO_2 during repeated opening of the reaction vessel for suspension withdrawal.

Results for total Fe (ICP-MS, UV-Vis) and Fe(II) (UV-Vis) in unfiltered and filtered suspensions from the replicate experiment are shown in Fig. EA7. Total Fe measurements showed good agreement between ICP-MS and UV-Vis data. Total Fe in unfiltered suspension slightly decreased over time, due to precipitate attachment to the wall of the reaction vessel. The evolution of the P/Fe ratio in the precipitate lost to the vessel wall closely matched the evolution of the P/Fe ratio of the precipitate isolated by filtration (not shown), suggesting that potential fractionation of different types of precipitates had not occurred to a significant extent. Comparison of Fe(II) and Fe_{tot} in the filtered suspension showed that "dissolved Fe" passing the filter membrane was mostly Fe(II). This suggested that colloidal Fe(III) was effectively retained by the filter membranes and that Fe passing the filter was mostly dissolved Fe(II). The difference between Fe(II) in the unfiltered and filtered suspension corresponds to Fe(II) in the precipitate. At the beginning and end of the experiment, this difference is very small and not reliably quantifiable. After 30 min and 60 min (where sample p-0-60 was collected; Fig. 6), Fe(II) accounted for ~23 and ~16% of the precipitated Fe. Since no measures were taken to avoid oxidation of the sample p-0-60 collected for analysis by XAS and TEM, the Fe(II) in the precipitate was likely oxidized to Fe(III) during sample separation and storage.

Fig. EA8. Suspensions from time-resolved experiment. Numbers indicate the time (min) after Fe(II) addition. Color evolution reflects initial formation of whitish-beige Fe-phosphate.

3. Mixing and sequential Fe(II) addition experiments: EXAFS spectra

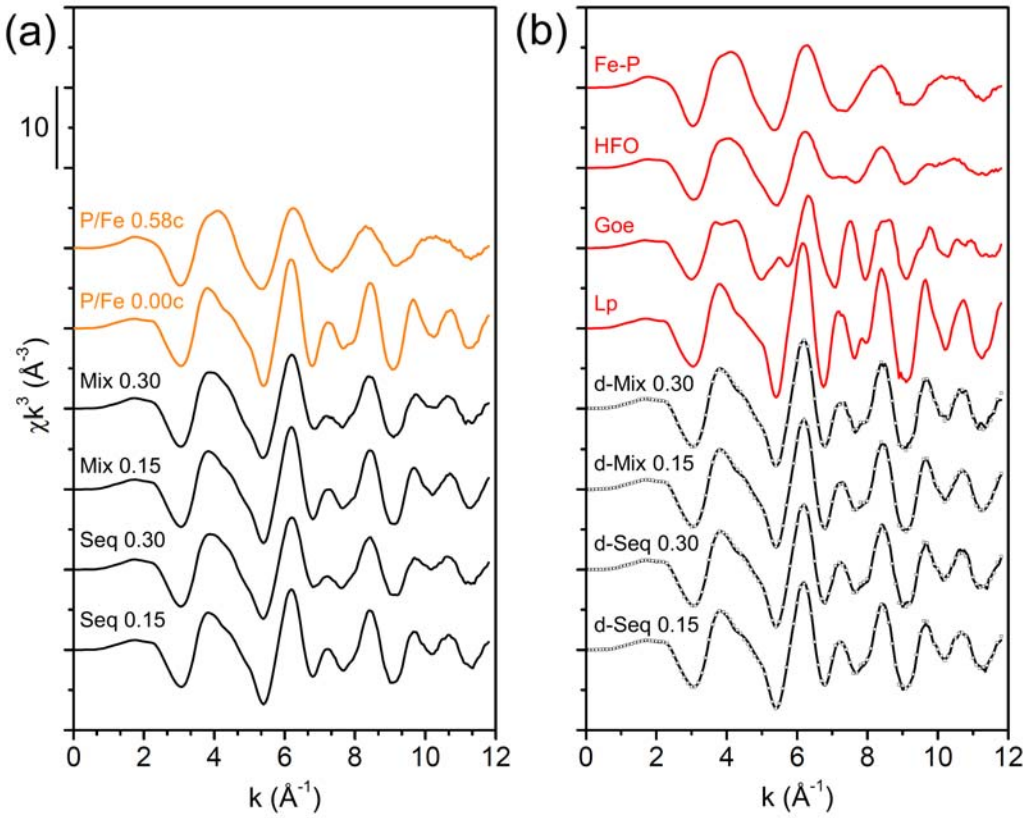

Fig. EA9. (a) Fe K-edge EXAFS spectra of starting precipitates from the mixing experiment and the final products of the mixing and sequence experiments (solid lines). (b) Fe K-edge EXAFS spectra of reference spectra, difference spectra (solid lines, calculated as described in section 3.3 and Table 3), and LCF spectra (open squares, LCF results in Table 3).

4. References

Carlson, L. and Schwertmann, U., 1990. The effect of CO_2 and oxidation rate on the formation of goethite versus lepidocrocite from an Fe(II) system at pH 6 and 7. *Clay Minerals* **25**, 65-71.

Cornell, R. M. and Schwertmann, U., 2003. *The Iron Oxides*. Wiley-VCH, Weinheim.

Villalobos, M. and Leckie, J. O., 2001. Surface complexation modeling and FTIR study of carbonate adsorption to goethite. *J. Colloid Interface Sci.* **235**, 15-32.